Evidence of Seattle Fault Earthquakes from Patterns in Deep-Seated Landslides

Erich Herzig*[1], Alison Duvall[1], Adam Booth[2], Ian Stone[3], Erin Wirth[3], Sean LaHusen[4], Joseph Wartman[1], and Alex Grant[3]

ABSTRACT

Earthquake-induced landslides can record information about the seismic shaking that generated them. In this study, we present new mapping, Light Detection and Ranging-derived roughness dating, and analysis of over 1000 deep-seated landslides from the Puget Lowlands of Washington, U.S.A., to probe the landscape for past Seattle fault earthquake information. With this new landslide inventory, we observe spatial and temporal evidence of landsliding related to the last major earthquake on the Seattle fault ~1100 yr before present. We find spatial clusters of landslides that correlate with ground motions from recent 3D kinematic models of Seattle fault earthquakes. We also find temporal patterns in the landslide inventory that suggest earthquake-driven increases in landsliding. We compare the spatial and temporal landslide data with scenario-based ground motion models and find stronger evidence of the last major Seattle fault earthquake from this combined analysis than from spatial or temporal patterns alone. We also compare the landslide inventory with ground motions from different Seattle fault earthquake scenarios to determine the ground motion distributions that are most consistent with the landslide record. We find that earthquake scenarios that best match the clustering of ~1100-year-old landslides produce the strongest shaking within a band that stretches from west to east across central Seattle as well as along the bluffs bordering the broader Puget Sound. Finally, we identify other landslide clusters (at 4.6–4.2 ka, 4.0–3.8 ka, 2.8–2.6 ka, and 2.2–2.0 ka) in the inventory which let us infer potential ground motions that may correspond to older Seattle fault earthquakes. Our method, which combines hindcasting of the surface response to the last major Seattle fault earthquake, using a roughness-aged landslide inventory with forecasts of modeled ground shaking from 3D seismic scenarios, showcases a powerful new approach to gleaning paleoseismic information from landscapes.

KEY POINTS

- Landslide clustering can record past earthquakes but requires known timing of a landslide inventory.
- New estimated landslide timing and modeled ground motions together reveal past Seattle fault earthquakes.
- This approach demonstrates a means to extract information on past earthquakes directly from landslide history.

Supplemental Material

INTRODUCTION

Strong ground motions from large earthquakes have long been known to trigger widespread landsliding (e.g., Keefer, 1984; Jibson and Keefer, 1993; Malamud *et al.*, 2004) that in some cases causes more economic destruction and human loss of life than from the primary earthquake shaking. Notable examples include the 1994 Paez, Colombia (Forero-Duenas, 1996) and 1997 Ardebil, Iran (Bird and Bommer, 2004) earthquakes. The Paez earthquake was an M_w 6.4 earthquake that triggered a large debris flow, which killed ~1100 people (Forero-Duenas, 1996). The M_w 7.4 Ardebil earthquake caused multiple landslides, some of which covered entire villages (Ishihara *et al.*, 1992). Earthquake-induced landslides can also set in motion an extended chain of surface processes and hazards, including persistent landslides and debris flows, dammed rivers, sediment aggradation, and floods in the days, months, and years

1. Department of Earth and Space Sciences, University of Washington, Seattle, Washington, U.S.A., https://orcid.org/0000-0002-3898-5971 (EH); https://orcid.org/0000-0002-7760-7236 (AD); https://orcid.org/0000-0001-7659-7198 (JW); 2. Portland State University, Portland, Oregon, U.S.A., https://orcid.org/0000-0002-7339-0594 (AB); 3. U.S. Geological Survey, Earthquake Science Center, Seattle, Washington, U.S.A., https://orcid.org/0000-0002-8592-4442 (EW); 4. U.S. Geological Survey, Geology, Minerals, Energy, and Geophysics Science Center, Moffett Field, California, U.S.A., https://orcid.org/0000-0003-4246-4439 (SLH)

*Corresponding author: eherzig@uw.edu

Cite this article as Herzig, E., A. Duvall, A. Booth, I. Stone, E. Wirth, S. LaHusen, J. Wartman, and A. Grant (2023). Evidence of Seattle Fault Earthquakes from Patterns in Deep-Seated Landslides, *Bull. Seismol. Soc. Am.* **114**, 1084–1102, doi: 10.1785/0120230079

following the initial seismic event (Fan *et al.*, 2019). Despite recent advances in our understanding of earthquake-induced hillslope failures, important questions remain regarding their expected number, size, distribution, and failure styles (e.g., Meunier *et al.*, 2008; Marc *et al.*, 2016; Croissant *et al.*, 2019; Valagussa *et al.*, 2019; Medwedeff *et al.*, 2020), as well as the longer term effects on hillslope geomorphology and sediment transport (e.g., Wartman *et al.*, 2013; Croissant *et al.*, 2019; Campforts *et al.*, 2020; Francis *et al.*, 2022).

Landslide properties, such as location and volume, are often coupled to the ground motion characteristics of the related earthquake (e.g., Jibson, 1985). Thus, studies of earthquake-induced landslides can also yield important paleoseismic information of past earthquake shaking (Jibson, 1996). One useful method for looking for past earthquake-induced landslides is by finding a cluster of related landslides in space and time (Crozier *et al.*, 1995). More recent studies suggest that the distribution of these landslide clusters can reveal patterns about where and when earthquake-induced landslides tend to occur in an area, as well as the seismic properties of the earthquake (Tanyas *et al.*, 2018; Wang *et al.*, 2020; Rasanen and Maurer, 2021). For example, Rasanen and Maurer (2021) propose a statistical approach that inverts probabilities of rupture location and magnitude from regional landslide evidence. Models of hillslope failures based on predictions of ground shaking intensity from 3D earthquake simulations (Allstadt *et al.*, 2013; Grant, 2017; Pollock *et al.*, 2019) may also yield insights into paleoseismic rupture parameters, especially when compared with patterns in documented landslide inventories.

Many of these approaches are improved as the number of landslides with an estimated age in an inventory increase. However, it is difficult to estimate the age of many landslides in a large inventory, and thus when studies of landslide geochronology (e.g., Aylsworth *et al.*, 2000; Brooks, 2013) are effective, these studies have also been somewhat few, especially the further back in time the earthquake occurred. Moreover, although it is increasingly common to develop a landslide inventory following a modern earthquake in locations where seismometers characterize the ground motions and earthquake properties (e.g., Tanyas *et al.*, 2018), it is much less common and more difficult to identify the cause of prehistoric landslides. Attempts at tying past landslides to seismic triggers typically involve geochronological dating that shows the landslide and earthquake were coincident, or slope stability models demonstrating that the landslide would never have failed unless there was seismic forcing (e.g., Jibson, 1996; Schulz *et al.*, 2012). This difficulty of studying older earthquake-induced landslides means that although we have a better understanding of earthquake-induced landslides in areas with large recent earthquakes (e.g., Aylsworth *et al.*, 2000; Brooks, 2013), other areas with infrequent earthquakes remain ambiguous.

In this article, we use the spatial and temporal patterns of landslides in the greater Seattle, Washington area of the United States to better understand past earthquakes on the Seattle fault zone (SFZ), a crustal fault that ruptures through this region. First, we present a newly mapped deep-seated landslide inventory of the Puget Lowland of Washington, a well-populated region that includes the city of Seattle and is notorious for landslide susceptibility and multiple drivers of hillslope instability (Tubbs, 1974; Coe *et al.*, 2004; Baum *et al.*, 2005; Schulz, 2007; Harp *et al.*, 2008; Davis *et al.*, 2022). Next, we apply a recently established method to estimate the ages of these landslides based on their surface roughness (LaHusen *et al.*, 2016; Booth *et al.*, 2017; LaHusen *et al.*, 2020). This method permits rapid assessment of the timing of thousands of deep-seated landslides on a regional scale. With this landslide inventory, we assess spatial and temporal landslide clustering as evidence of the last major Seattle fault earthquake, which ruptured to the surface around 1050–1020 cal B.P. (Bucknam *et al.*, 1992; Atwater, 1999; Sherrod, 2001; Nelson *et al.*, 2014). We then compare this clustering with a suite of simulated M_w 7.0 earthquakes on the Seattle fault (Stone *et al.*, 2022) to explore possible earthquake characteristics, including regions of strong ground motion, based on the landslide record.

PUGET LOWLAND STUDY AREA AND BACKGROUND

Seattle and the surrounding area lie within the Puget Lowlands of Washington, U.S.A. (Fig. 1), a region where landslides pervade the landscape (Laprade *et al.*, 2000; Washington Geological Survey, 2020). High regional landslide susceptibility stems from the many steep slopes underlain by weak glacial material (Tubbs, 1974; Schulz, 2007; Perkins *et al.*, 2017), a wet maritime climate, proximity to earthquake-producing faults, and human activity. Compilations of historical landslides (Laprade *et al.*, 2000; Washington Geological Survey, 2020) show a predominance of precipitation-induced landslides in this region. Recorded landslides have been paired with complementary precipitation data to estimate rainfall and soil moisture conditions that lead to shallow slope failures in Seattle (Baum *et al.*, 2005; Godt *et al.*, 2006). New Bayesian modeling of landslide inventories indicates that the highest probability of precipitation-induced landslides occurs on January or February, just after the annual precipitation peak (Luna and Korup, 2022).

In contrast to precipitation-induced landslides, earthquake-induced landslides are much less frequent or predictable in this area. In fact, no large ($>M_w$ 5) earthquakes on surface faults in the Puget Lowlands have happened during the modern record (1900–2023). The few earthquakes that have occurred in the historical record (1900–2023) were deep intraslab earthquakes with strong, but not severe, ground motions (peak ground velocity [PGV] <50 cm/s, see Data and Resources). The most recent of these was the 2001 M_w 6.8 Nisqually earthquake that induced few landslides in the region (Highland, 2003). However, significantly more landslides are expected for

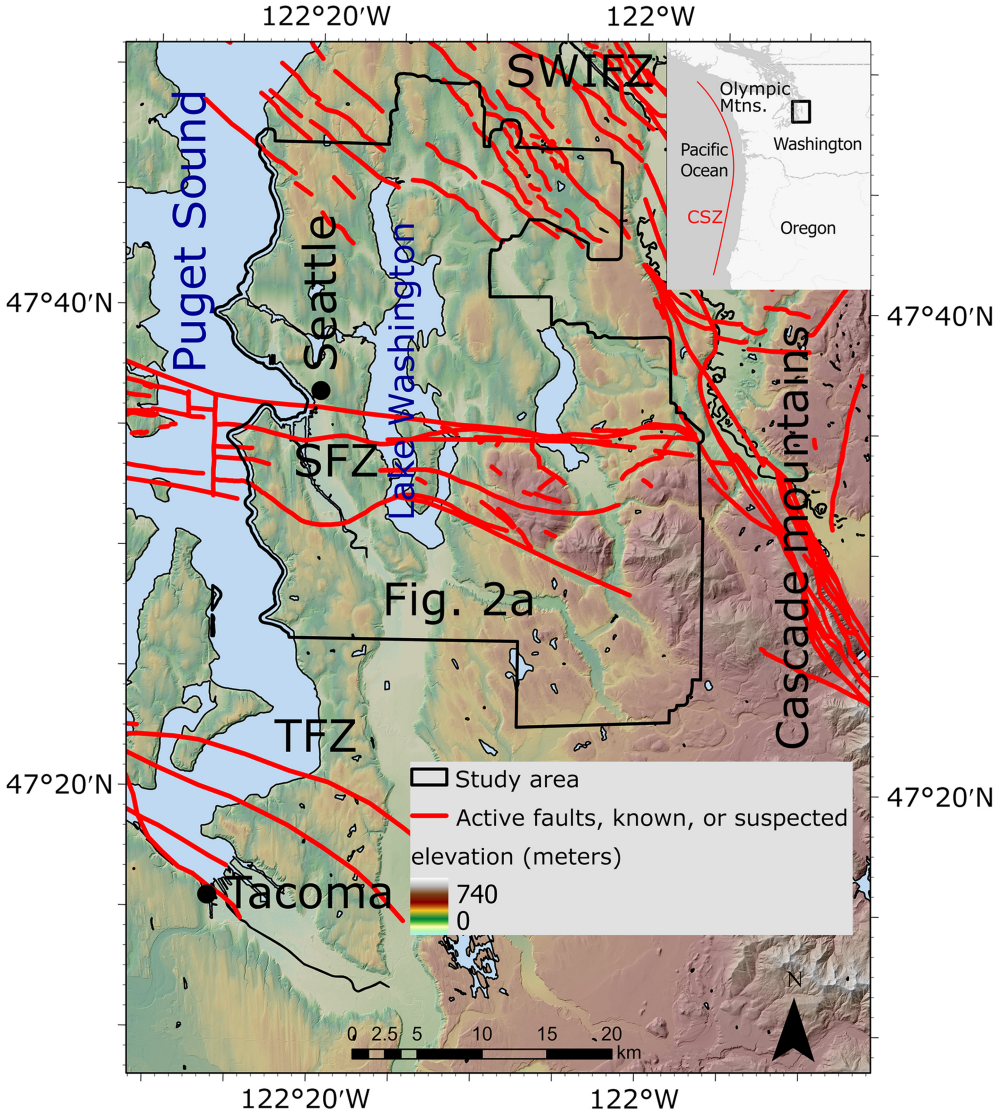

Figure 1. Shaded-relief map of the Puget Lowlands, highlighting the study area. The black outline shows the region of mapped landslides, shown in Figure 2, and the red lines are mapped active faults (see Data and Resources). TFZ is the Tacoma fault zone, SFZ is the Seattle fault zone, and SWIFZ is the southern Whidbey Island fault zone. Inset map shows location in Washington State, U.S.A., and relation to the Cascadia Subduction Zone (CSZ) in red. The color version of this figure is available only in the electronic edition.

M_w~9 Cascadia subduction zone (CSZ) earthquakes, and more still from ruptures near the surface on crustal faults (Grant, 2017). Here, we focus on the Seattle fault (also known as SFZ), a crustal fault zone running through the City of Seattle (Fig. 1) with a recurrence interval for a full rupture on the SFZ of longer than 6500 yr (Sherrod *et al.*, 2000). Other earthquakes recorded with paleoseismic data in the SFZ occur more frequently and are still large enough (M_w 6.5–7) to induce landsliding (Nelson *et al.*, 2003, 2014; Karlin *et al.*, 2004). The SFZ is one crustal fault of several in the Puget Lowlands fault inventory that also includes the southern Whidbey Island fault (Johnson *et al.*, 1996, 2004; Sherrod *et al.*, 2008) to the north and the Tacoma fault (Brocher *et al.*, 2001; Sherrod *et al.*, 2004) to the south (Fig. 1).

The SFZ is an active south-dipping crustal reverse fault within the forearc of the CSZ that trends east–west for 60–65 km across the Puget Lowlands (Johnson *et al.*, 1999; Blakely *et al.*, 2002; Fig. 1). The locations, orientations, and dip of SFZ splays are poorly constrained (e.g., Pratt *et al.*, 1997; Johnson *et al.*, 1999; Brocher *et al.*, 2001; ten Brink *et al.*, 2002; Moore *et al.*, 2022). The three main fault strands of the SFZ are blind (Johnson *et al.*, 1999; Blakely *et al.*, 2002); however, secondary backthrusts within the hanging wall of the main structure break the surface, forming Holocene fault scarps (Nelson *et al.*, 2003, 2014; Kelsey *et al.*, 2008). The current best estimate, derived from dendrochronology, of the last major SFZ earthquake is that it occurred in the winter of 1093–1092 yr B.P. (Black *et al.*, 2023) and had an estimated magnitude of 7–7.5 (ten Brink *et al.*, 2006, Styron and Sherrod, 2021). This earthquake triggered regional uplift (Bucknam *et al.*, 1992) and a tsunami in the Puget Sound (Atwater and Moore, 1992). The SFZ also had at least one more recent earthquake, and possibly several others. Nelson *et al.* (2014) identified earthquake "NE" at 940–380 cal B.P. and Angster *et al.* (2022) identified earthquake "RH2" at <530 cal B.P. These earthquakes were likely only partial ruptures and were smaller than the earthquake that occurred ~1000 yr ago. In the last 4000 yr, the SFZ has also had at least three older earthquakes: earthquake "RH1," ~1330 cal B.P. (Angster *et al.*, 2022), earthquake "NC," 1310–1200 cal B.P. (Nelson *et al.*, 2003, 2014) and earthquake "NB," 2650–1940 cal B.P. (Nelson *et al.*, 2003, 2014). These earthquakes likely had magnitudes around M_w~7 (Nelson *et al.*, 2003, 2014).

Landslide deposits within Lake Washington (Jacoby *et al.*, 1992; Karlin *et al.*, 2004), as well as within the Olympic mountains to the west (Schuster *et al.*, 1992), along with oral histories of SFZ-associated ground failures (Ludwin *et al.*, 2005),

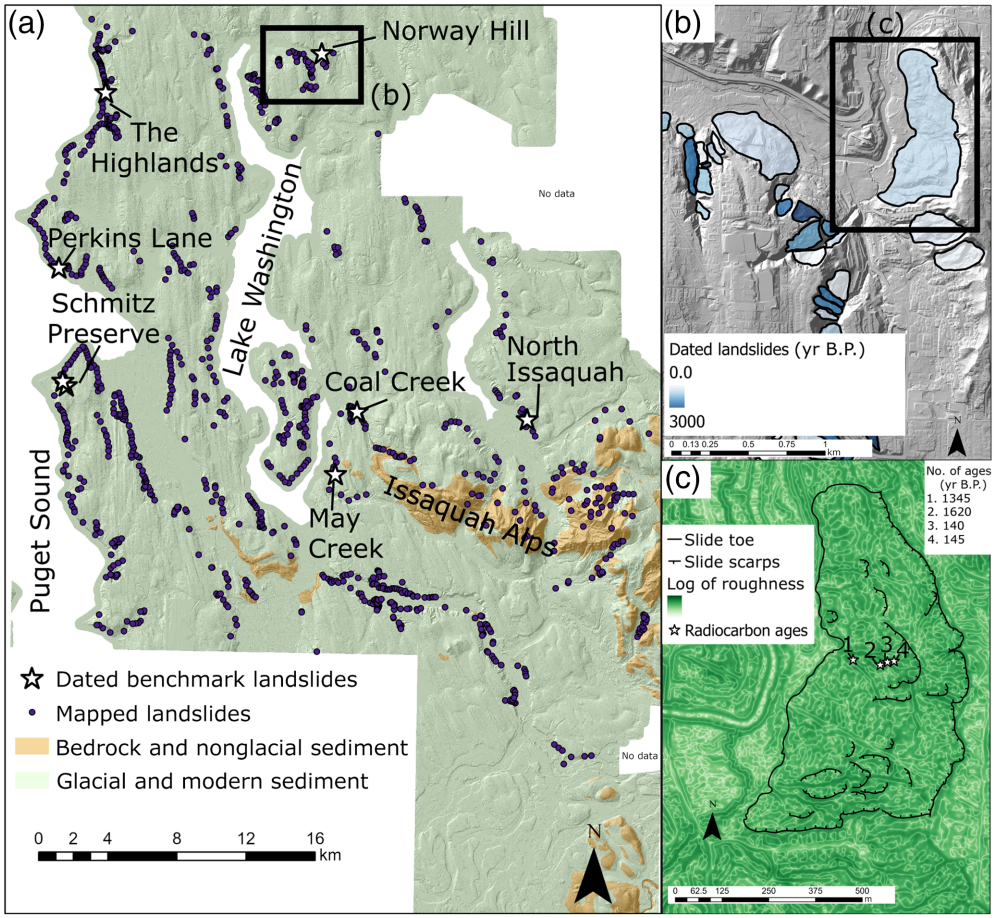

Figure 2. Landslide inventory maps. (a) Light Detection and Ranging (lidar) hillshade map with all mapped deep-seated landslides from this study as circles and benchmark (dated) landslides as stars. The map is colored based on whether the surface geologic unit is glacial, modern, or bedrock (Yount *et al.*, 1993). (b) Lidar hillshade map with a subset of mapped landslide areas colored by roughness-based age. See panel (a) for location. (c) Roughness map showing landslide toe and scarps of a benchmark landslide. Radiocarbon sampling locations are numbered and shown with stars; corresponding mean ages are in a table in the top right corner. See panel (b) for location. The color version of this figure is available only in the electronic edition.

implicate a strong landscape response to earthquakes in the region. The full impact of earthquake-induced ground shaking on hillslopes from past SFZ earthquakes; however, remains poorly resolved. Allstadt *et al.* (2013) modeled where future landslides might occur using a single scenario SFZ earthquake simulation. This work was useful for revealing how site and basin amplification may control where earthquake-induced landsliding occurs in the Seattle area, leading to increased landslide rates in the Seattle basin and in areas with unconsolidated sediments. They also found that higher ground saturation (100% versus 0% saturation) would lead to about an order of magnitude more landslides.

Using a similar methodology, Grant (2017) analyzed the hillslope response to simulated CSZ megathrust earthquakes and found that an earthquake on the SFZ would likely cause more landslides in the Seattle area than a CSZ earthquake.

The findings of Allstadt *et al.* (2013) and Grant (2017) have yet to be vetted against a record of past landslides due to limited information about the timing or cause of the thousands of discrete, deep-seated landslide deposits that exist within the landscape. By mapping, dating, and characterizing spatial patterns of the deep-seated landslides, we improve our understanding of the distribution of earthquake-induced landslides in the area. In addition, we compare our landslide inventory with a new suite of SFZ earthquake scenario simulations (Stone *et al.*, 2022), to assess possible earthquake properties of past earthquakes on the SFZ.

METHODS

Landslide mapping and dating

Using high-resolution (1 m) Light Detection and Ranging (lidar) data (see Data and Resources), we mapped over 1000 deep-seated landslides in the Puget Lowlands area (Fig. 2, Table S1, available in the supplemental material to this article). Throughout the rest of this article, when we refer to landslides from this inventory, we are specifically referencing deep-seated landslides, those in which the slide plane lies below the roots of trees. Such deep-seated landslides are often categorized as rotational or compound landslides using the classification system of Hungr *et al.* (2014). Landslide deposits were mapped from bare-earth lidar imagery based on the presence of headscarps, many of them arcuate, upslope of hummocky terrain (Fig. 2). Previous mapping by Washington Geological Survey geologists was used as a reference point (Washington Geological Survey, 2020). Lidar data were used to calculate properties of these mapped landslides, such as height (from headscarp to deposit toe) and length of the landslide. Field observations, including stratigraphy and morphology assessments at some of the landslides, confirmed the accuracy of the remote mapping. Field observations were combined with lidar-based mapping to create detailed morphology maps of a selection of benchmark landslides that were dated using radiocarbon ages (Fig. 2c).

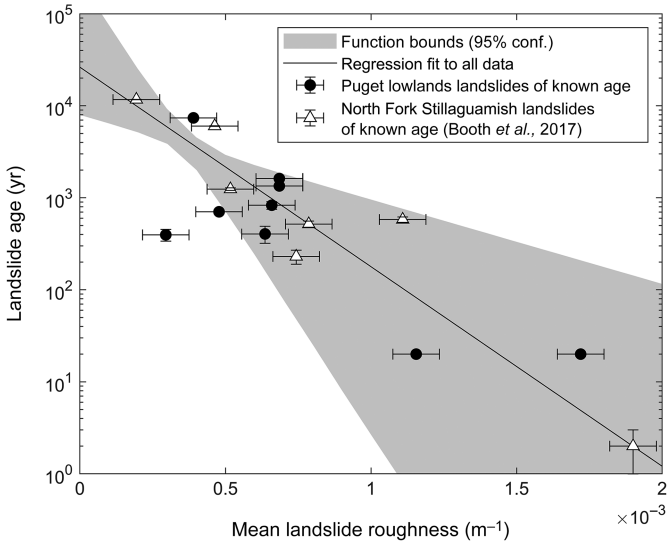

Figure 3. Age-roughness relationship for the Puget Lowlands. Previous data from the North Fork Stillaguamish Valley (Booth *et al.*, 2017) are shown as triangles and new data from landslides from the Seattle region of the Puget Lowlands (this study) are shown as circles. The exponential fit to data from both datasets is plotted as a black line with the shaded area indicating uncertainty on this fit (95% confidence bounds). Uncertainty was calculated by varying input data based on their error and refitting the exponential fit, the gray area then shows where 95% of these functions cover.

To provide age information for our full catalog of landslides, we applied a recently developed method based on the age-calibrated roughness of landslide deposits (LaHusen *et al.*, 2016; Booth *et al.*, 2017). The premise behind this method is that the ground surface roughens significantly from mass movement. As a result, landslide deposits exhibit their highest roughness just after failure and smooth by diffusive hillslope processes over time (e.g., Fig. S1). This smoothing can be modeled as an exponential age-roughness relationship (Fig. 3). Calibrating this relationship for the field site requires measured roughness values for each landslide deposit and several benchmark landslides of known age. The lidar we used was collected in 2016, so here this roughness method provides an age before 2016. For this reason, when analyzing and discussing landslide timing within this article, we use yr B.P. starting at 2016.

Following Booth *et al.* (2017), we measured landslide roughness using a 15 m Ricker wavelet (Ricker, 1943) transform, often known as a "Mexican hat" wavelet, on the lidar elevation data of the landslide deposit (Booth *et al.*, 2009, 2017; LaHusen *et al.* 2020). This wavelet was scaled so that it measures topographic curvature as a function of length scale (Kumar and Foufoula-Georgiou, 1997; Lashermes *et al.*, 2007; Booth *et al.*, 2017). We used a 15 m scaled wavelet based on work by Booth *et al.* (2017) showing that this length scale best-characterized landslide age in a similar topographic, climatic, and sedimentologic setting north of our study area. We excluded areas of the deposit within 8 m of places that have been altered in ways not modeled by simple soil diffusion, such as gullies or roads. Gullies were identified as areas with a concave-up profile curvature of >0.09 m^{-1} and with a drainage area of >2670 m^2 calculated using a D-infinity flow accumulation algorithm as done in Booth *et al.* (2017). Landslide roughness may vary as a function of failure style, relative activity, or material properties (McKean and Roering, 2004; Booth *et al.*, 2009, 2017; Goetz *et al.*, 2015). To minimize these effects, we considered only deep-seated rotational landslides within similar glacial materials. By controlling for landslide type and parent material, we assume landslide deposits included in this study will be governed by similar diffusive relationships. Landslides mapped as failing in different styles, or from different parent materials were excluded from this study. Some mapped landslides are also active, with many landslides exhibiting reactivation. For consistency, we map complex landslides as a single slide. Although the error on the age for a single landslide is high, making it difficult to definitively estimate the age of a single slide, the quantity of landslides with estimated ages allows for studying large-scale patterns.

To establish newly dated benchmark landslides to calibrate the roughness model, we used radiocarbon dating of organic material embedded in the landslide deposits. We targeted streams incised into landslide deposits to collect nine pre-modern (pre-1950) samples of wood and other organic debris. We only took samples that were entrained within the landslide deposit to minimize the chance that they are not associated with the main landslide failure. Radiocarbon dating is well suited to the landslides of the study area because abundant vegetation is likely to be preserved in landslide deposits, but it does have some disadvantages (Pánek, 2015). For example, many landslides are part of large landslide complexes that have failed many times. These reactivations can contain both new material and older material from past landslides, and as such, their radiocarbon ages can be difficult to interpret. In addition, sample material such as charcoal can be older than landslides that contain it (Struble *et al.*, 2020). To reduce this uncertainty, we collected multiple samples when possible. By comparing these ages, as well as looking to lidar to identify crosscutting relationships (Ramsey, 2009), we constrain the ages of some of these landslides to a smaller range than that provided by just a single sample. These samples were dated using accelerator mass spectrometry (AMS), performed by DirectAMS. Calibrated ages were derived using OxCal version 4.3.2 (Ramsey, 2017) with IntCal13 (Reimer *et al.*, 2013).

We combine radiocarbon data from the North Fork Stillaguamish (LaHusen *et al.*, 2016; Booth *et al.*, 2017), which lies in a similar climate to the Puget Lowlands and has similar Quaternary glacial deposits, with the newer Puget Lowlands landslide ages to develop the age-roughness relationship that we use in this study: $t = 26{,}298 \times \exp(-4{,}994r)$ in which t is the time in yr B.P. and r is the roughness in m^{-1} (Fig. 3).

TABLE 1
Modeled Earthquake Scenarios

Hypocenter Location	Slip Distribution Number 1	Slip Distribution Number 2	Slip Distribution Number 3
West hypocenter	Scenario 1	Scenario 4	Scenario 7
Central hypocenter	Scenario 2	Scenario 5	Scenario 8
East hypocenter	Scenario 3	Scenario 6	Scenario 9

We then use this function to estimate the age of all landslides in our inventory. The final ages are subject to multiple sources of uncertainty. The radiocarbon ages have error based on both the radiocarbon dating and the time that passed between wood growth and entrainment into the landslide deposit. The roughness measurements themselves are variable based on the lidar data quality, and may differ between landslide styles. These sources of error are then incorporated into uncertaintity of the age-roughness relationship (gray area in Fig. 3) and thus the final landslide ages.

Landslide history models

We adapt a landslide history model developed by LaHusen *et al.* (2020) to assess the main causes of landsliding in the area from 4600 yr B.P. to present day. This model considers the effects of variable initial landslide deposit roughness on the roughness-based age calculation, as well as the effect of preservation bias. It produces a count of landslides in a given area over time. This helps us understand if the variations we see in the landslide chronology are the result of natural variation, bias, and error, or if there is an underlying signal. Because of the uncertainty of the roughness ages and the nonlinear relationship between roughness and age, an earthquake is unlikely to be represented by a sharp peak in landslide frequency, but instead by a broad peak (LaHusen *et al.*, 2020). We can model this sort of broad peak and compare it with the landslide inventory to test if it is present in our data. We used two model setups and compare these with the observed landslide history: one with steady landslides and one that also included pulsed landslides. The model pair allows us to consider the possible impacts of earthquake-induced landslides on the landslide record. For each model, we ran 10,000 simulations to explore the possible range of starting roughness values. A baseline annual landslide rate was used to approximate landslides caused by precipitation and other landslide triggers in the steady model. It is worth noting that precipitation-induced landslides are not actually constant through time, but stochastic and likely subject to a heavy-tailed distribution of interevent times (e.g., Sadler, 1981; Schumer and Jerolmack, 2009). Although the low precision of the landslide ages should mitigate the error from a steady assumption, this does represent a potential source of unmeasured error. This baseline rate was also included in the earthquake-pulse model, which added an additional earthquake-induced landslide factor modeled as a pulse of landslides observed at the time of the last major earthquake on the SFZ (~1100 yr B.P., Sherrod *et al.*, 2000).

Other earthquake sources have produced earthquakes that likely impacted the study area during this time period, most notably several M_w~9 CSZ earthquakes (Goldfinger *et al.*, 2012). Although these M_w~9 earthquakes may have induced landslides in the study area, this earthquake signal is not easily identified due to uncertainty in the landslide dating method and the frequency of earthquakes (LaHusen *et al.*, 2020). For this reason, we focus on the SFZ, which is most proximal to the study area, ruptures to the surface, and has a longer recurrence interval such that landslide signals from each earthquake do not overlap. In addition, the overlapping signals from M_w 9 earthquakes should not disrupt our ability to measure signals from a SFZ earthquake because they are implicitly included in the background landslide rate. The upper age limit of 4600 yr B.P. and 200 yr bins were chosen by limiting our focus to bins that contain at least five landslides. Because we are only considering the last 4600 yr and the last major shift in climate in this area occurred 6000 yr B.P. (Cwynar, 1987), we assume that the climate, and thus the baseline background landslide rate, remained relatively consistent during this period and would have had a less significant impact on the landslide history than earthquakes. However, we are not restricting the ages used to calibrate the age-roughness relationship (which include ages up to ~10,000 yr) and thus a change in climate may be a source of uncertainty in our age-roughness relationship. Preservation bias is modeled as an exponential function fit to the landslide frequency derived from the inventory. This bias is multiplied by the modeled landslide frequency to show what might be observed in a real world landslide inventory.

In addition to landslide frequency through time, we also model landslide areas using a power law relationship $p(x) \propto x^{\alpha}$, in which α is an exponent derived from the frequency–area distribution of the landslide inventory, p is the probability of occurrence, and x is the area of the landslide, as developed in Tanyas *et al.* (2018). We do this using the methods described in Clauset *et al.* (2009). This provided a power law exponent of −1.8 with a cutoff at 6600 m^2. Landslide frequency–area distributions are known to only follow a power law at larger areas, whereas smaller landslides below a rollover point do not (e.g., Malamud *et al.*, 2004; Frattini and Crosta, 2013). To avoid issues with modeling this rollover point, we conservatively only simulate landslides with areas >9000 m^2.

The two landslide history models described earlier, one background steady-state model and one earthquake (pulsed) model, were tuned to match the total number of landslides in the mapped landslide inventory. This tuning was done to minimize the error between the model and the inventory

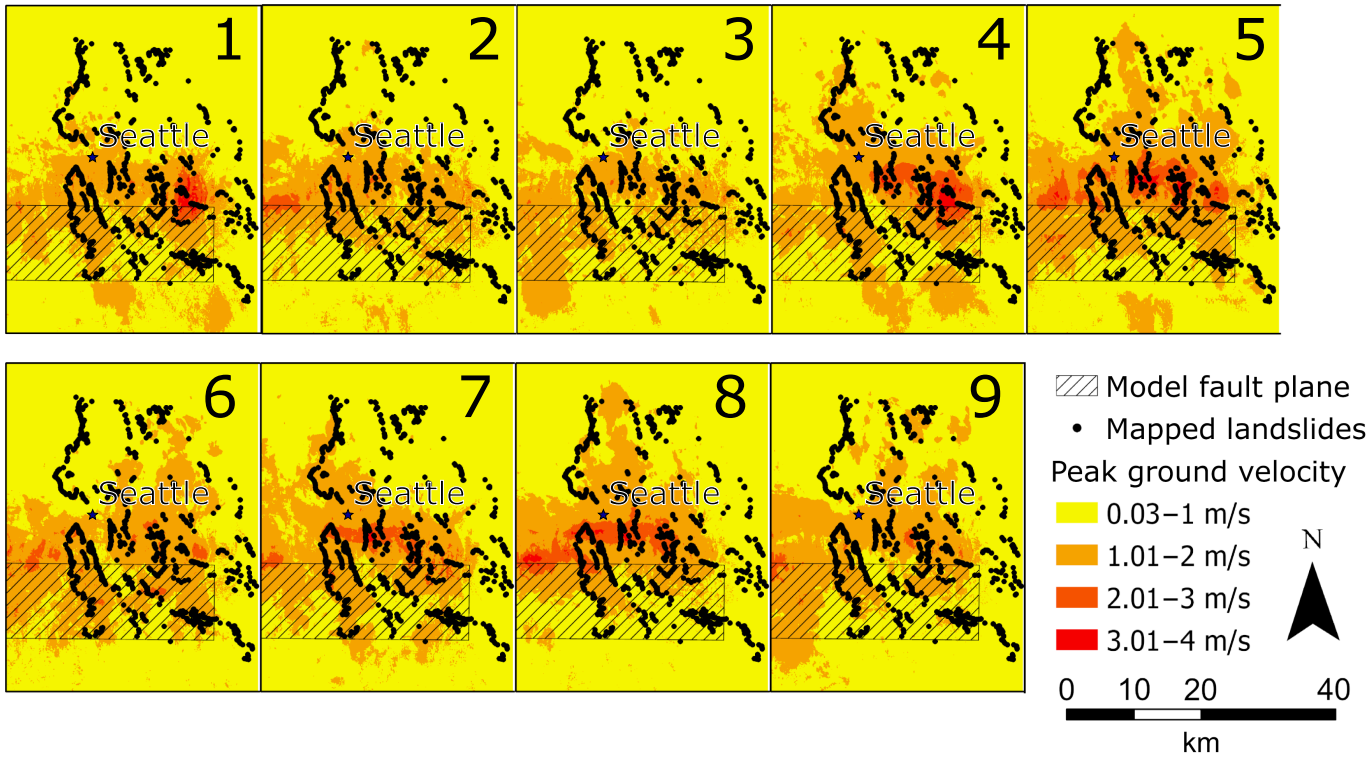

Figure 4. Ground motions in peak ground velocity (PGV) for each SFZ earthquake scenarios (1–9). Higher ground motions are indicated with red and orange; and lower ground motions in yellow. The landslide inventory is shown as points and the modeled fault plane location shown as a cross-hatched rectangle. The color version of this figure is available only in the electronic edition.

(Fig. S2). We restricted this tuning to the modeled window of 400–4600 yr B.P. to remove the effect of apparent increase of landslides in the past 400 yr. The resulting number of landslides is different than the total number of landslides created by the model because of preservation bias, which has been noted in similar studies (LaHusen *et al.*, 2016, 2020; Booth *et al.*, 2017).

SFZ earthquake simulations

We use nine simulations of SFZ earthquakes to compare landslide clustering with modeled ground motions and use these comparisons to invert for reasonable ground motion characteristics of the last major earthquake on the SFZ (~1100 yr B.P.). The ground motions we use are PGVs from nine different M_w 7 scenario earthquakes on the SFZ (Fig. 4; Stone *et al.*, 2022). We use PGV instead of peak ground acceleration (PGA) due to limitations of the simulations for producing accurate PGA values. These models incorporate the effects of topographic amplification as well, an important element for understanding landslide initiation. The nine different rupture scenarios we consider (Table 1) are based on a combination of three different slip distributions (Fig. 5) and three different hypocenter locations (east, center, and west), as described in detail by Stone *et al.* (2022). The three slip distributions were randomly generated but can roughly be described as slip concentrated in the east (distribution 1), in the west (distribution 2), and in the central portion of the rupture (distribution 3).

The spatial distribution of observed landslides among different PGVs from the SFZ earthquake simulations is measured using a probability density function (PDF) created using a kernel density smoothing function. First, two PDFs were created, one for the occurrence of landslides P(Landslide) and another for the distribution of PGVs P(PGV). We also create a conditional probability of PGVs in areas with landslides P(PGV|Landslide). Using Bayes' theorem, we can then calculate the probability of landsliding at a given PGV P(Landslide|PGV). To consider areas that landslides are likely to occur, these distributions were derived only for areas with slopes higher than 10°. This cutoff was chosen based on proportionally fewer landslides occurring on slopes <10° (Fig. S3). PGV distributions were based on median PGV values from all scenarios, to avoid being skewed by a single scenario with a high PGV at any given location; though, a mean PGV-based analysis produces similar results. The spatial distribution of these median peak ground motions is shown in Figure 6, along with the landslide inventory. We exclude the higher PGV values in which P(PGV) ≤ 0.1, because the low sample sizes at these values lead to misleading statistics. We also calculated the conditional probability P(Landslide|DistanceFromFault) in a similar manner, finding the probability of landsliding given a 3D distance

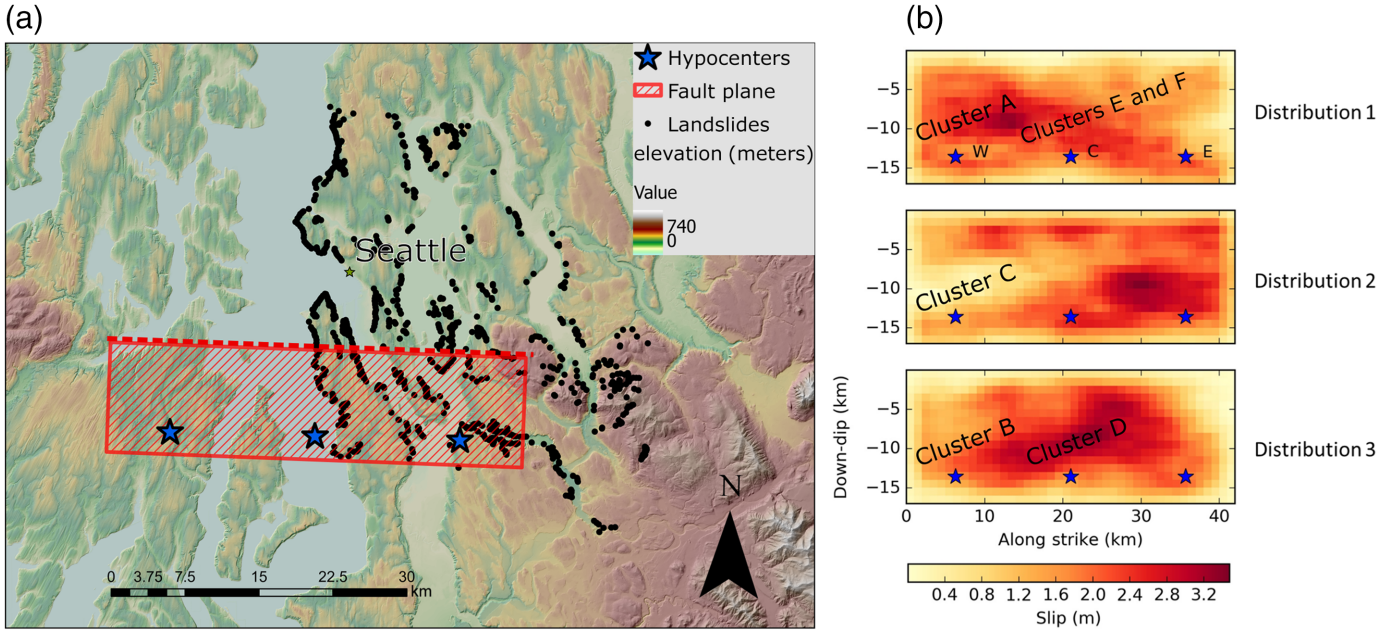

Figure 5. Properties of considered earthquake scenarios. (a) Shaded relief map with scenario fault plane (red) and hypocenter locations (blue stars) with mapped landslide inventory shown as black points. (b) Slip distributions and hypocenter locations (stars, W indicates west, C indicates central, and E indicates east) for all scenarios (adapted from Stone *et al.*, 2022). Best-fit scenarios for different temporal landslide clusters (A–F) are highlighted (see the Results, Discussion, and Figure 9 for details). The color version of this figure is available only in the electronic edition.

from the modeled fault plane. We perform these measurements for both observed landslide count and observed landslide area. Landslide area weights the statistics, so that larger landslides have a larger effect on the probabilities.

To test for spatial clustering of landslides based on earthquake shaking (PGV), or distance to rupture, we use a two sample Kolmogorov–Smirnov (K–S) test. This technique tests if two sample sets are drawn from the same nonparametric continuous probability distribution (Massey, 1951). In our case, we compare the background distribution of PGV, representing earthquake shaking intensity, across all landslide-susceptible areas within our study, with the distribution of PGVs just within mapped landslide polygons. From global empirical observations (Keefer, 1984; Jibson, 1985; Malamud *et al.*, 2004), we assume areas of stronger shaking should promote more, and larger, landslides compared with areas of less shaking, and construct a null hypothesis to test that the distributions of PGV in both landslide and nonlandslide points match. Given this assumption, we use the K–S test to identify two conditions: (1) the null hypothesis is rejected, and landslide polygons show a significant difference in PGV compared with background; or (2) we cannot reject the null hypothesis and landslides are not sensitive to high (or low) PGV values. K–S tests were performed on landslide distributions for a sequence of 200 yr time periods from 0 to 4.6 ka using all nine SFZ earthquake simulations. We hypothesize that during periods of local ground shaking due to SFZ earthquakes (e.g., around the most recent 1093–1092 yr B.P. event, Black *et al.*, 2023), we will observe a strong clustering of landslides in high-PGV regions and reject the null hypothesis, whereas in aseismic periods, we will observe more uniformly distributed precipitation-induced landsliding and will not reject the null hypothesis. We ran the K–S test two times for each time period, once measuring if the distribution of landslides correlated with ground motions, and once to see if the landslides exhibit an inverse relationship with ground motions. We use results from this test to interpret whether the landslides in each of these time periods were likely to be caused by ground motions from one of the scenario earthquakes. This is useful because even if a temporal cluster is caused by precipitation or another earthquake source (such as the southern Whidbey Island fault), it will not show up in this test (i.e., the spatial distribution of landslides will not correlate with the likely spatial distribution of PGV from a SFZ earthquake). In this way we can narrow the source of the landslide cluster to just those likely caused by a SFZ earthquake. The inverse test, on the other hand, will not represent earthquake-induced landslides. Instead, this test measures if there are more landslides in areas with low PGVs. Such a pattern could be expected if landslides that occur in the years after an earthquake are preferentially located in areas that did not fail during the previous earthquake.

RESULTS

New radiocarbon ages

To develop our roughness relationship (Fig. 3), we dated six benchmark landslides using AMS radiocarbon dating

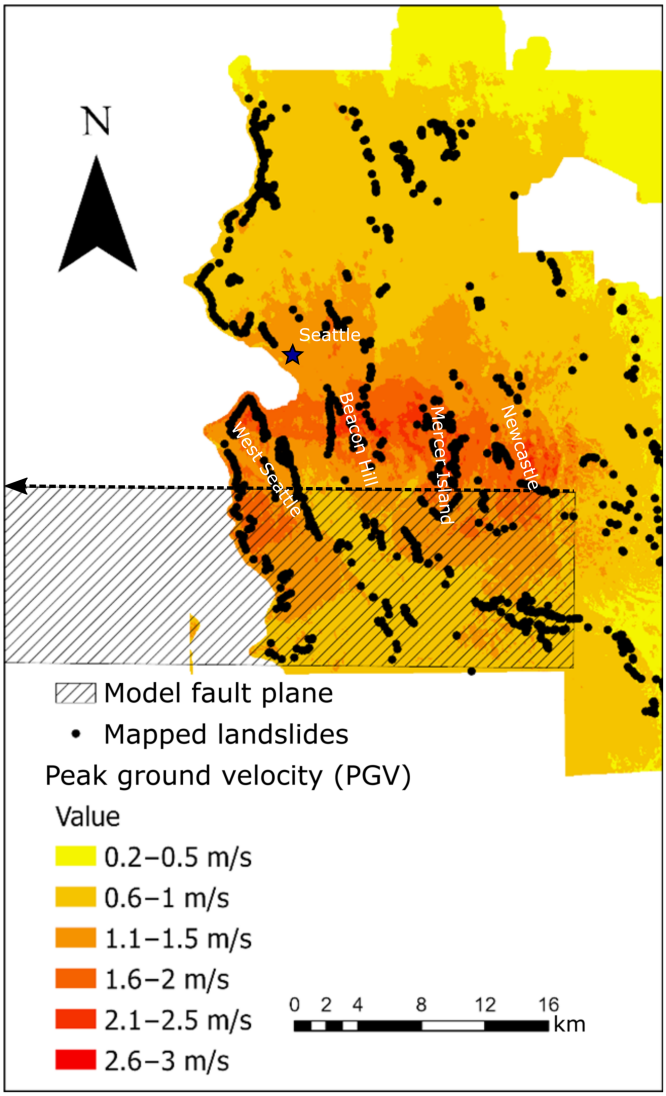

Figure 6. PGV map for the study area based on median maximum horizontal ground motions from all earthquake model scenarios. Mapped landslides are shown as points. The fault plane is shown as the hatched area, with a dashed line showing the surface trace of the fault. The arrow indicates that the fault trace and plane continue to the west out of the frame. The color version of this figure is available only in the electronic edition.

performed by DirectAMS (Table 2). Four ages are from the Norway Hill landslide complex (Fig. 2). These ages, derived from samples of wood and other organic materials, were collected from exposed gullies running up the complex and were, in order from lowest to highest elevation sampling loca tion: 1345 ± 45, 1620 ± 80, 140 ± 140, 145 ± 145 cal B.P. Uncertainty on these and other dates is 2-sigma error. Based on crosscutting relationships observed from the lidar data in which younger landslides overlay older landslides, the youngest two ages likely represent a more recent secondary failure in the landslide complex, whereas the older two likely represent the initial age of the complex. For this reason, we use both older dates to calibrate the age-roughness model (Fig. 3), but not the younger ages. Although these ages do not overlap in error and may represent separate failures, they are close enough that excluding either does not significantly change the age-roughness fit.

We also obtained two ages from wood buried in individual landslides in the Schmitz Preserve, with ages of 405 ± 85 and 7390 ± 70 cal B.P. for landslides in the northern and eastern parts of the preserve, respectively (Fig. 2a). We also obtained one age from wood exposed in a gully near May Creek (Fig. 2a), which gave an age of 396 ± 58 cal B.P for that landslide. Two additional charcoal ages were obtained from landslides near North Issaquah (830 ± 80 cal B.P.) and Coal Creek (705 ± 25 cal B.P.; Fig. 2a). Owing to long preservation times, charcoal is more likely to provide a maximum age constraint than an absolute age. However, based on the relatively young ages recorded here, we used these to calibrate the age-roughness relationship. Finally, to consider the youngest possible ages, we use landslides that occurred during the winter of 1996–1997 at Perkins Lane and near the "Highlands" (Fig. 2a; Baum *et al.*, 1998).

Landslide inventory

We mapped 1064 deep-seated landslides in the study area (Table S1). Geographic information systems polygons of our mapped landslide inventory are available as a shapefile with the supporting information. Some of these landslides are part of slide complexes with multiple successive failures. Individual landslides range in area from 300 to 530,000 m^2, with a mean landslide size of 18,000 m^2. The height-to-length ratios (height is measured as base of headscarp to end of toe) of the landslides range from 0.03 to 4, with a mean height-to-length ratio of 0.5. The landslides generally occurred along the steep slopes of the area, such as waterfront bluffs and river valleys (Fig. 2a) and overlap with areas predicted to fail in a SFZ earthquake by Allstadt *et al.* (2013) and Grant (2017). We did not map bedrock failures in the Issaquah Alps (Fig. 2a), which explains the dearth of landslides from that region in our inventory.

The landslide inventory ages, derived from roughness, reflect an exponential preservation bias, with more landslides having younger ages owing to the erosional removal and overwriting of older landslide deposits (Fig. 7, Table S1). This appears as a linear relationship in the semilog plot in Figure 7. However, there are even more landslides at younger ages than this bias would predict, with a large increase in landslides with ages younger than 400 yr B.P. This may be an artificial increase due to the "Sadler effect" (Sadler, 1981; Schumer and Jerolmack, 2009), in which changing the sampling window can artificially increase measured rates of stochastic events (see the supplemental material and Fig. S4 for more information on this effect). Beyond the expected preservation bias and Sadler effect, there are additional fluctuations in the number of landslides through time, such as around 1.0 and 2.6 ka (Fig. 7).

TABLE 2
Benchmark Landslide Radiocarbon Ages

Landslide Name	Material	Radiocarbon Age (yr B.P.)	1σ Error (yr)	Calibrated Ages (cal B.P.) with 2σ Error*	Latitude and Longitude
North Issaquah slide	Charcoal	903	22	830 ± 80	122°2′39.47″W and 47°33′36.725″N
Schmitz Preserve north	Wood	382	23	405 ± 85	122°245.205″W and 47°34′36.04″N
Schmitz Preserve east	Wood	6484	36	7390 ± 70	122°23′57.341″W and 47°34′27.28″N
Norway Hill	Wood	1463	24	1345 ± 45	122°12′24.437″W and 47°44′58.484″N
Norway Hill	Wood	1706	37	1620 ± 80	122°12′20.92″W and 47°44′58.089″N
Norway Hill	Wood	161	20	140 ± 140	122°12′20.102″W and 47°44′58.356″N
Norway Hill	Wood	173	25	145 ± 145	122°12′19.215″W and 47°44′58.452″N
Coal Creek	Charcoal	789	20	705 ± 25	122°10′16.695″W and 47°33′41.193″N
May Creek	Wood	317	21	396 ± 58	122°11′25.899″W and 47°31′49.360″N

*Calibrated ages from OxCal (4.3.2) using IntCal13 and are in years before 1950. Additional information in Table S2.

Modeled landslide histories through time

The results of the roughness-based landslide models through time are shown in Figure 7 and compared with the inferred frequency of landslides from our inventory (black line). Because these models only consider landslides >9000 m^2, the landslide inventory is similarly filtered to provide an appropriate comparison. The steady model has a landslide rate of 16 landslides per 100 yr. The best-fit earthquake (pulsed) model has a landslide rate of 12 landslides per 100 yr with 80 additional landslides induced by simulated representation of the last major SFZ earthquake. Both of these best fits are determined by minimizing root mean square logarithmic error (rmsLE) between the modeled frequency distributions and the observed landslide distribution.

Although the earthquake-induced landslide model produces an overall similar pattern to the steady landsliding model, it does do a better job of fitting some of the observed variations in landslide frequency and area. Based on comparing the frequency distributions of the models with the observations, the earthquake model has an rmsLE of 0.018, and the steady model has an rmsLE of 0.078. For the area distributions, these errors are 0.54 and 2.8, respectively. In particular, the earthquake landslide model fit is better around the time of the last major SFZ earthquake ~1100 yr B.P. in the area distribution. Although the fit is also slightly better for the earthquake model in the frequency distributions, it is less robust. Both models fail to capture a cluster in landsliding around 2.6 ka and 3.8–4.6 ka, possibly related to other SFZ earthquakes (Nelson *et al.*, 2003; Karlin *et al.*, 2004). These peaks might be better characterized by a model with landslides induced from those earthquakes. We did not try to replicate the substantial increase in modern landsliding observed in the last 400 yr. This cluster may be a result of the Sadler effect (Sadler, 1981; Schumer and Jerolmack, 2009), see the supplemental material and Figure S4.

SFZ earthquake simulations and spatial landslide patterns

Assuming that spatial correlations between landslides and PGV signify earthquake-induced landslides, we can use the spatial distribution of landslides to measure the likelihood that landslides were earthquake induced. Spatial patterns were first assessed by comparing landslide distributions with PGVs and distance to the fault. Although conditional landslide probability is proportional to distance from the fault and PGV, the relationship is stronger for PGV with higher maximum probabilities for both landslide count (conditional probability for PGV 0.144 > conditional probability for distance 0.071) and area (conditional probability for PGV 0.116 > conditional probability for distance 0.082; Fig. S5). As a result, we use PGV as the main indicator of earthquake-induced landslides. It should also be noted that P(Landslide|PGV) stops being a useful indicator at high PGVs (P(PGV) ≤ 0.1) due to their low probability of occurrence. The distribution of P(Landslide|PGV) at different 200 yr intervals is shown in Figure 8 (Fig. S6 is similar but uses mean PGV instead of median PGV). Highlighted in this figure are time periods that have higher than average correlations between landslides and PGV (blue and yellow lines), the time slice that includes the last known major SFZ earthquake (red line), and the "null" time slice of the last 200 yr, a time window that we know did not experience a major SFZ earthquake.

Using the D statistics produced by two sample K–S tests, we compare the ground motions from different scenarios with the spatiotemporal distribution of landslides in Figure 9 and Table 3. The D statistic is a measure of how different the probability distributions of the two samples are, with higher values corresponding to greater differences. Above a critical value this statistic invalidates the null hypothesis that the two samples are from the same distribution. This critical value varies based on the input sample size but is on average ~0.1 at a 99.9% confidence level for our dataset. Any value higher than this is considered statistically significant. We can additionally compare the values to get a relative measure of how well the distributions agree. To better compare variability in critical values among the different scenarios, Table 3 lists the D statistic divided by the corresponding critical value and Figure 9 summarizes this by finding the average normalized D statistic over

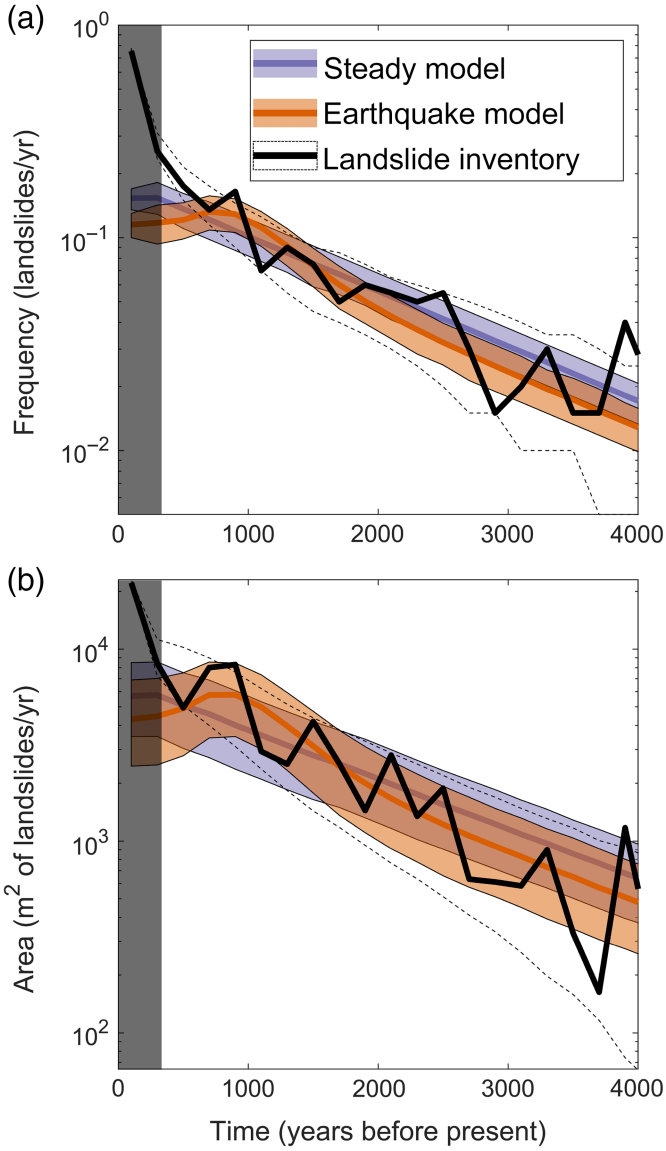

Figure 7. (a) Landslide frequency and (b) area over time. The black line represents the mapped landslide inventory, 2σ error in dashed lines. The dark gray vertical bar over the most recent time interval indicates the anomaly, possibly due to the Sadler effect, that is not considered during modeling. The blue line and shaded area represent the model with a uniform landslide rate. The orange line and area represent the model with an increase in landslide frequency and area around the time of the last major earthquake on the SFZ. The lines indicate the mean values, and the shaded areas represent 90% of model runs. See the Methods section for scenario model details. The color version of this figure is available only in the electronic edition.

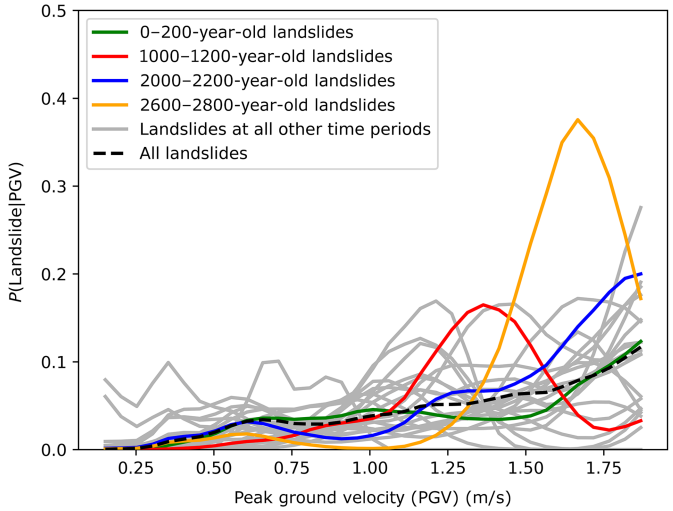

Figure 8. Conditional probability of landsliding as a function of PGV *P*(Landslides|PGV) at 200 yr time slices. Highlighted time slices are in color: green for 0–200 yr B.P., red for 1000–1200 yr B.P. (time window that includes a known SFZ earthquake), blue for 2000–2200 yr B.P., and yellow for 2600–2800 yr B.P. Other time slices from 4.6 to 0 ka are plotted in gray. The probability for the entire time period is plotted as a dashed black line. PGV is from the median of all earthquake scenarios in units of m/s. The 0–200 period represents a "null" scenario because no M_w 7.0 earthquakes from faults in the region have been recorded, felt, or described during this time. The blue and yellow highlighted time slices have the maximum conditional probabilities. The color version of this figure is available only in the electronic edition.

all scenarios for each time period. We interpret values higher than 1 to indicate some earthquake-induced landslides, with higher values corresponding to a higher likelihood and proportion of earthquake-induced landslides. We plot (Fig. 9) both the positive correlation (solid line with points) and inverse correlation (dashed line with points). The positive correlation between the landslides and PGV values represents earthquake forcing, whereas a lack of correlation or inverse correlation may represent landslides triggered by other forces. Inverse correlation additionally may suggest some sort of preconditioning of the landscape by earthquakes, causing landslides in areas other than those that failed due to shaking. These values may not visually match the patterns shown in the conditional probability plots (Fig. 8), because small number statistics can artificially inflate the conditional probability at high PGVs (e.g., the 2.8–2.6 ka event in Fig. 8).

By comparing across time, we look for high positive correlation values to indicate that an earthquake likely occurred during a given period. Moreover, by comparing across scenarios during that interval (Fig. S7), we estimate the most likely distribution of ground motions from that simulated earthquake scenario. We observe the highest normalized D statistics in the 1.2–1.0 ka and 1.0–0.8 ka time periods, which correspond to the time of the last major SFZ earthquake (peak labeled B in Fig. 9). Within these time periods, earthquake scenario 7 (Table 1, Fig. 4), from 1.2 to 1.0 ka, has the highest D statistic among the different scenarios considered. This scenario was generated using a western hypocenter and slip distribution 3, with centrally concentrated slip (Table 1, Fig. 5). The spatial distribution of PGV from scenario 7 shows the strongest ground motions in a band stretching from West Seattle to Mercer Island (Fig. 4, scenario 7). Relative to other scenarios, this scenario also has higher ground motions along the bluffs bordering the Puget Sound.

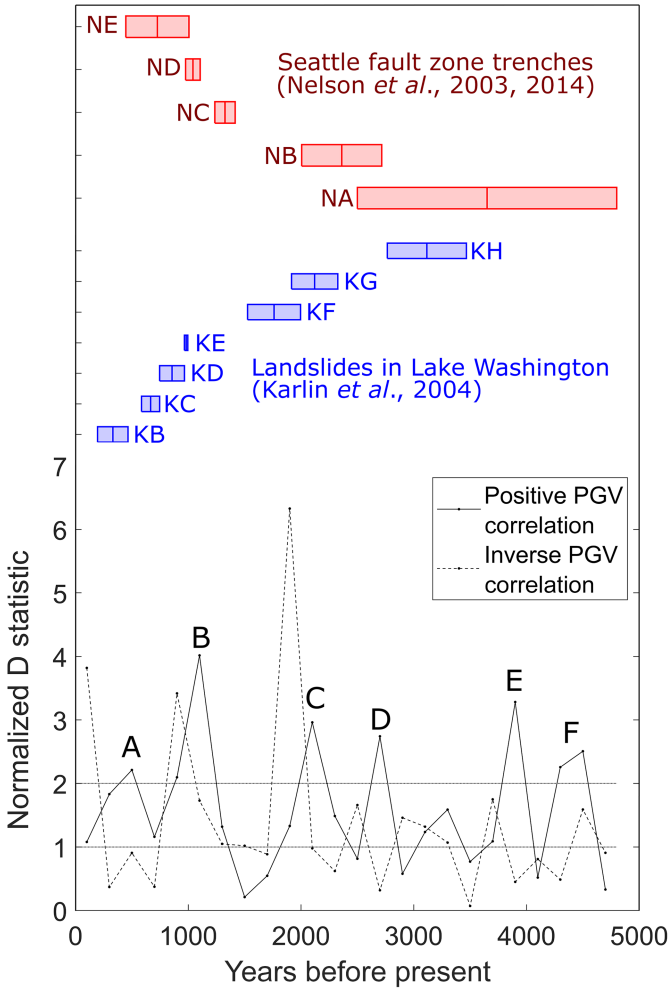

Figure 9. Plot showing the normalized D statistic (D statistic divided by the corresponding critical value, D statistic compares landslide distribution and PGV distribution) averaged over the nine earthquake simulation scenarios for each 200 yr time interval through 4800 yr B.P. Horizontal lines show values of 1 and 2. Values above 1 invalidate the null hypothesis and indicate earthquake forcing. Values above 2 have a higher probability of earthquake forcing and are used to designate possible earthquakes. These clusters are labeled (A–F); cluster B overlaps with the timing of the last major SFZ earthquake. See Discussion for details. For comparison, other earthquakes on the SFZ (Nelson *et al.*, 2003, 2014) are plotted as red bars (labeled NA-NE) and landslide deposits in Lake Washington (Karlin *et al.*, 2004) are plotted as blue bars (labeled KA-KH). The color version of this figure is available only in the electronic edition.

We can also look for other clusters in the normalized D statistic that indicate other possible earthquakes (value > 2). As a check on this approach, we inspect the most recent 200 yr, an interval in which no significant earthquakes were recorded along the SFZ. As expected, we find no spike or corresponding increase in the normalized D statistic to indicate any earthquake-induced landslide activity. Consideration of older time intervals shows evidence for one cluster younger and four clusters older than the ~1100 yr B.P. SFZ earthquake (B in Fig. 9). We name the clusters in increasing age as A (0.6–0.4 ka), B (1.2–0.8 ka), C (2.2–2.0 ka), D (2.8–2.6 ka), E (4.0–3.8 ka), and F (4.6–4.2 ka; Fig. 9, Table 3). The slip and hypocenters of the best-fitting scenarios for each of the clusters are presented in Figure 5 and the expected ground motions are presented in Figure 4.

DISCUSSION

The new deep-seated landslide inventory presented here combined with landslide age and earthquake ground shaking scenario models substantiates that the landscape records past earthquakes on crustal faults in the Seattle region. Each line of evidence examined supports the inference that earthquake-induced landsliding led to temporal and spatial clustering of landslide deposits in the study area, at least for the last M_w~7 SFZ earthquake (~1100 yr B.P.). Although this interpretation can be drawn from either the temporal or spatial datasets separately, the most robust conclusions come from considering all the data and models together. The discovery of landslide clustering due to earthquakes is important over both geologic and human timescales because such patterns should affect landscape evolution and hazards in the region. Our results differ from work by LaHusen *et al.* (2020), which found little evidence that deep-seated landslides within the Oregon Coast Range are triggered by subduction zone earthquakes. This may be due to stronger ground motions and less seismic wave attenuation from crustal fault earthquakes, as opposed to subduction earthquakes. Although CSZ earthquakes may have higher moment magnitude, they are typically deeper and offshore, and thus generally have lower PGVs at inland sites (Serey *et al.*, 2019). Alternatively, the presence of a fault damage zone in the crustal SFZ could be at play, which has been shown to affect earthquake-induced landslide patterns in other fault zones (e.g., Bloom *et al.*, 2022) and there are differences in radiated frequency content among crustal versus subduction zone earthquakes.

The observed temporal pattern of landslide ages in the Puget Lowland fits slightly better to a model with a pulse of landslides at the time of the last major SFZ earthquake rather than steady landslides through time (Fig. 7). In addition, a model based on the landslide area distributions fits better than the frequency distributions. This indicates that a consideration of landslide area through time can help identify an earthquake signal. Perhaps this is due to some differences in size from different landslide sources, although this variation is difficult to resolve with our dataset (see Fig. S8, which shows a constant landslide area power law exponent through time, suggesting no source dependence for landslide size). However, it is worth noting the uncertainty in resolving an earthquake signal from landslide age-modeling alone. In both plots that we consider, landslide frequency and landslide area (Fig. 7), the fits to the earthquake model are not perfect and it is possible that the cluster we interpret as an earthquake signal ~1000 yr ago may be

TABLE 3
K–S Test Normalized D Statistics for Different Earthquake Scenarios, Time Periods, and Earthquakes from Paleoseismology Studies

Age Range (Years Ago)	Scenario 1	Scenario 2	Scenario 3	Scenario 4	Scenario 5	Scenario 6	Scenario 7	Scenario 8	Scenario 9	Mean	Cluster from This Study	Nelson *et al.* (2003, 2014) Earthquakes	Karlin *et al.* (2004) Events
0–200	2.371	1.343	0.807	0.876	1.294	0.664	1.378	0.297	0.690	1.080			B
200–400	1.690	2.424	1.498	2.017	1.959	1.854	2.089	2.161	0.788	1.831			B
400–600	2.339	1.161	1.938	2.401	2.648	2.416	2.488	2.580	1.927	2.211	A	E	
600–800	1.138	0.806	1.052	1.072	1.556	1.378	1.031	0.681	1.736	1.161		E	C
800–1000	1.969	1.164	1.193	2.623	1.221	3.082	2.608	3.005	1.999	2.096	B	E	D
1000–1200	4.917	2.470	4.656	3.559	4.647	3.292	5.328	4.137	3.144	4.017	B	D	E
1200–1400	0.763	0.653	1.009	2.071	1.872	1.120	1.597	1.716	1.083	1.320		C	
1400–1600	0.216	0.431	0.322	0.301	0.099	0.147	0.055	0.047	0.284	0.211			F
1600–1800	0.211	0.065	0.000	0.879	0.942	0.520	0.766	1.546	0.000	0.548			F
1800–2000	0.999	1.099	1.870	0.922	1.590	1.272	1.846	1.779	0.601	1.331			F and G
2000–2200	1.638	3.397	1.436	4.419	3.225	1.641	4.051	3.643	3.208	2.962	C	B	G
2200–2400	1.686	1.787	0.599	1.112	1.751	2.012	1.250	0.989	2.203	1.487		B	G
2400–2600	0.661	0.078	0.823	1.934	0.578	0.162	1.209	1.273	0.622	0.816		B	
2600–2800	2.957	2.253	2.056	2.262	3.253	2.999	3.300	3.408	2.194	2.742	D	A	H
2800–3000	0.239	0.590	0.908	1.171	0.726	0.107	0.483	0.489	0.510	0.580		A	H
3000–3200	1.390	1.528	1.931	1.145	0.231	1.988	1.256	0.922	0.740	1.237		A	H
3200–3400	0.913	1.561	0.591	1.519	2.092	2.053	1.607	2.155	1.805	1.588		A	H
3400–3600	0.985	0.278	0.945	1.043	0.826	0.661	0.660	0.688	0.849	0.771		A	H
3600–3800	0.735	1.008	1.025	0.824	1.508	1.133	0.859	1.215	1.508	1.090		A	
3800–4000	2.111	4.208	2.767	2.660	3.516	2.956	3.445	3.798	4.094	3.284	E	A	
4000–4200	0.386	0.314	0.363	0.952	0.376	0.679	0.625	0.463	0.526	0.520		A	
4200–4400	2.185	3.764	1.983	1.962	1.715	1.342	2.119	2.248	2.997	2.257	F	A	
4400–4600	3.091	3.861	2.492	2.648	2.194	2.278	1.829	2.232	1.943	2.508	F	A	
4600–4800	0.336	0.374	0.589	0.346	0.136	0.282	0.223	0.168	0.517	0.330		A	

K–S, Kolmogorov–Smirnov.

noise. In addition, our focus on landslides with areas greater than >9000 m^2 may bias the distribution and miss some pattern in smaller landslides. In addition, when our models assume a relatively constant background rate, even precipitation-induced landslide events tend to be stochastic (Coe *et al.*, 2004). This means that our models do not account for the Sadler effect (Sadler, 1981; Schumer and Jerolmack, 2009), seen in the inventory dataset (see the supplemental material). The large uncertainties on individual landslide ages associated with the age-roughness dating approach limit our ability to identify high-magnitude landslide-triggering earthquakes in the record, especially if they occur somewhat frequently. In theory, infrequent large earthquakes, such as along the SFZ, should be distinguishable in the landslide record, whereas more frequent earthquakes will blur together and be indistinguishable from the background rate. In practice, this means the landslide timing record cannot be used to rule out the occurrence of earthquakes due to an absence of temporal clustering and the strongest conclusions can be made when combining landslide age information with spatial patterns (e.g., Grant *et al.*, 2022). In addition, it is worth noting that some of the earthquake-induced landslides may not be triggered coseismically, but instead fail in the following years after an earthquake main shock due to aftershocks or weakened slope materials.

In our study, we also see a trend in the spatial clustering of landslides that comports with ground shaking modeled for past earthquakes on the SFZ (Stone *et al.*, 2022; e.g., Fig. 6). Given similarities in geologic material and mean annual precipitation across the study area, we expect spatial patterns of nonseismic landslides to be relatively unclustered and random through time. Future work may be able to compare our deep-seated landslide inventory with modern shallow landslide inventories to test if this assumption is true for nonseismic landslides. In contrast, when looking at specific time periods for our dataset, we observe a significant shift in the spatial pattern of landsliding that we interpret to record earthquake activity (Fig. 8). This shows that earthquake-induced landslides do not affect the entire study area equally and will have different effects in different areas. In addition, there is a mismatch in the distribution of interpreted nonseismic and earthquake-induced landslides (0–200–year-old versus 1000–1200–year-old landslides in Fig. 8). This observation has implications for landslide hazard assessments because hazard based on rainfall-based predictions, for example, will not necessarily correlate with hazard from earthquake-induced landslides.

By comparing the spatial landslide distribution with the modeled PGVs in different scenarios, we can look for an indication that an earthquake occurred during that time interval, as well as determine the best-fitting patterns in ground motions during the last major earthquake on the SFZ. We do this using the K–S D statistic as a measure of how different a given landslide distribution is from the norm, which for a positive correlation indicates the likelihood that a landslide distribution is caused by an earthquake scenario. For the 1.2–1.0 ka and 1.0–0.8 ka intervals, the period that includes the last known major rupture on the SFZ, all ground motion scenarios show positive correlation D statistics well above the critical value (Fig. 9, Table 3). None of the earlier time intervals show scenarios this high above the normalized critical value of 1. These results show strong evidence that spatial landslide patterns were impacted by an earthquake during this time. Although any of the scenarios are statistically reasonable based on the normalized critical value, the scenario that best matches the landslide distribution (scenario 7) has the strongest ground shaking stretching from West Seattle to Mercer Island, with strong shaking along the bluffs of the Puget Sound. This scenario was created using a western hypocenter and central slip distribution.

We next speculate on the earthquake properties from other identified possible earthquakes using the best-fit scenarios, with the caveat that the nine earthquake scenarios considered do not represent a full suite of potential rupture characteristics. Many of the landslide clusters found in our data may represent the same earthquakes recorded in fault trenches in the SFZ (Nelson *et al.*, 2003, 2014) and turbidite and landslide deposits in Lake Washington (Karlin *et al.*, 2004; Fig. 9). Cluster A (0.6–0.4 ka) correlates with earthquake NE (940–380 cal yr. B.P) from Nelson *et al.* (2014). This may also represent RH2 (650–200 cal B.P) noted by Angster *et al.* (2022). Cluster A does not have a clear best-fit ground motion scenario, with most scenarios performing equally well (Fig. S7). Cluster C (2.2–2.0 ka) correlates with earthquake NB (2650–1940 cal B.P) from Nelson *et al.* (2003, 2014) and event KG (2260–1850 cal B.P) from Karlin *et al.* (2004). The best-fit scenario (Fig. S7) for this cluster indicates the strongest ground motion from Beacon Hill to Newcastle (Fig. 6), with high ground motions along the Puget Sound on the western edge of the study area. Cluster D (2.8–2.6 ka) may represent earthquake NA (>2500 cal B.P) from Nelson *et al.* (2003, 2014) and event KH (3400–2700 cal B.P) from Karlin *et al.* (2004). The best scenario (Fig. S7) for cluster D had the strongest motions stretched from West Seattle to Mercer Island (Fig. 6), with relatively high ground motions around Lake Washington. Cluster E (4.0–3.8 ka) overlaps, as well, with earthquake NA (>2500 cal B.P) from Nelson *et al.* (2003, 2014). This cluster has some of the lowest ground motions of any scenario, with strong shaking mostly confined to the area near the surface trace of the fault. The 4.6–4.4 ka and 4.4–4.2 ka increases (cluster F) also overlap with earthquake NA (>2500 cal B.P) from Nelson *et al.* (2003). This cluster also has a best fit (Fig. S7) to the same scenario as cluster E, which suggests that E and F might be a signal from the same earthquake. Based on the best fits to all these clusters (Fig. S7), an eastern hypocenter appears least likely to have

occurred in the past 4600 yr, when all other hypocenters and all slip distributions tend to be the best fit for at least one possible earthquake.

Some proposed earthquakes from Nelson *et al.* (2003, 2014), Karlin *et al.* (2004), and Angster *et al.* (2022) are not apparent in our landslide inventory. Karlin *et al.* (2004) date submarine landslide and turbidite deposits in Lake Washington and interpret some of these to be seismically induced. Although the SFZ is proximal to this lake, other triggers, such as large storms (e.g., Karlin *et al.*, 2004 event KD [900–680 cal B.P.]) or earthquakes on other faults or the CSZ (e.g., Karlin *et al.*, 2004 event KB [400–130 cal B.P.]), could lead to such deposits. In contrast, Nelson *et al.* (2003, 2014) studies and Angster *et al.* (2022) are directly linked to the SFZ because they trenched a backthrust. One possible explanation for why we could miss an event would be if dry conditions during the rupture led to fewer landslides and a less diagnostic spatial pattern. This may explain why we do not see a clear signal from earthquake NC (1350–1170 cal B.P.) from Nelson *et al.* (2003, 2014) and why there is also no landslide signal in Lake Washington at that time (Karlin *et al.*, 2004). To this point, Allstadt *et al.* (2013) tested both dry and wet hillslope conditions and found that the total area of landslide sources was an order of magnitude smaller when an earthquake happened during the dry season than when soils were completely saturated.

The D statistic for the inverse correlation may also contain information regarding these past earthquakes. Only three time periods (2.0–1.8 ka, 1.0–0.8 ka, and 0.2–0 ka) have inverse D statistics higher than 2, and all of these postdate landslide clusters C, B, and A, respectively. This may represent a delayed effect in which after an earthquake has caused landslides on unstable slopes with strong shaking, the remaining unstable slopes will be biased toward areas that experienced less shaking. In the following centuries this pre-existing bias could lead to an apparent inverse relationship between landslides and ground motions during periods with no earthquakes. This conflicts with other studies (e.g., Parker *et al.*, 2015) showing that earthquake-induced landslide locations are influenced by past failures, and are more likely in areas that failed in the past. Perhaps the triggering mechanism is important here, with earthquake-induced landslides occurring more frequently in the same locations, whereas rainfall-induced landslides are more likely in areas without earthquake-induced landslides. Further testing of this hypothesis could help improve our understanding.

Taken together, these results can be tentatively interpreted to indicate that the SFZ does not have a characteristic rupture style and instead generates earthquakes with a variety of slip distributions, hypocenter locations, and resulting ground motion distributions. Although this means that we cannot rule out any rupture parameter for either past or future earthquakes on the fault, we can assess the likelihood of different ground motion distributions in the past based on the landslide record. For example, based on our analyses, we can show that an eastern hypocenter is the least likely hypocenter location for these past earthquakes. An important caveat to this interpretation is that ground motions are not unique to a particular set of rupture parameters and the modeled likelihoods will not fully contain the rupture parameters to a single set of values. The ground motions also used a uniform shear-wave velocity minimum of 450 m/s, instead of a more detailed consideration of variations in glacial sediment site effects (see the supplemental material for more discussion on the ground motion simulation parameters). In addition, the different scenarios all have sufficiently different PGV distributions such that risk analyses based on a single earthquake scenario may obscure the interevent variability of seismic hazard due to SFZ earthquakes. Because of these factors, future work using this method could be improved by considering a wider range of earthquake scenarios, with more variability and granularity in the rupture parameters. For example, when Stone *et al.* (2022) considers three different hypocenters, they are all at the same depth on the fault. Considering different hypocenter and rupture depths could expand the range of possible ground motions we use to evaluate earthquake-induced landslides.

CONCLUSIONS

In this study, we combine analysis of a new, deep-seated landslide inventory with morphologically estimated ages, with landslide and earthquake simulation modeling to investigate spatial and temporal clusters of landslides in the Puget Lowlands of Washington State, U.S.A. We find evidence of increased landsliding around the time of the last major SFZ earthquake. Spatially, this corresponds to more landslides in areas with higher modeled PGVs. Temporally, this increase in landslides leads to possible clustering with ages near the time of the last major SFZ earthquake. By restricting our view to landslides within the timeframe of the 1050–1020 cal B.P. SFZ earthquake (Bucknam *et al.*, 1992; Atwater, 1999; Sherrod, 2001; Nelson *et al.*, 2014), we also see an increase in spatial clustering compared with the temporally unrestricted spatial patterns. Landslide clustering also reveals evidence of earlier earthquakes on the SFZ, some of which correlate with other paleoseismic evidence (Nelson *et al.*, 2003, 2014; Karlin *et al.*, 2004). Our work helps to refine the ages for these past earthquakes. Earthquake NA (>2500 cal B.P.) from Nelson *et al.* (2003) is poorly constrained, and when we cannot narrow it down to a single time period, we can suggest that it may be related to either landslide cluster D (2.6–2.8 ka), E (3.8–4.0 ka), or F (4.2–4.6 ka). In addition, comparison of different earthquake scenarios with the landslide inventory identifies the modeled ground motions that best match the clustering related to the last major SFZ earthquake. We find that the scenario with

strongest shaking stretching from West Seattle to Mercer Island and high shaking along the bluffs bordering the Puget Sound fits best. This scenario (i.e., scenario 7) was created with a western hypocenter and central slip distribution. By applying this technique to the other possible earthquake-induced landslide clusters, we see that a variety of different ground motion distributions provide the best match to different temporal landslide clusters (Fig. S7), which suggests that SFZ earthquakes have variable rupture characteristics that result in different patterns of ground shaking. More generally, our study demonstrates the power of combining a regional landslide inventory with multiple earthquake scenario models to perform paleoseismic analysis. Future work in the Puget Lowland could investigate if there are similar landslide clusters related to other crustal faults such as the southern Whidbey Island fault. Our approach offers a means to investigate past earthquakes, especially in areas with rare, but strong earthquakes in landscapes prone to landsliding. In which records of past seismic activity are missing, the method may be used as one of the few means to extract information about past earthquake ground motions directly from the landscape.

DATA AND RESOURCES

The supplemental material contain additional details about the Seattle fault earthquake simulations and the temporal landslide model. It includes testing for a scale-based preservation bias and the Sadler effect. It also contains a data table of all 1000+ landslides with estimated ages and a shapefile of all landslides. Faults in Figure 1: Bowman, J. D., and Czajkowski, J. L. (2019). Washington State seismogenic features database—GIS data: Washington Geological Survey Digital Data Series 1, version 5.0, previously released April 2016 available at https://gis.dnr.wa.gov/site1/rest/services/Public_Geology/Earthquake/MapServer. Light Detection and Ranging (lidar): lidar Bare-Earth digital elevation model (DEM) [computer file]. (2016). Corvallis, Oregon, U.S.A.: QSI Corvallis, available at: Puget Sound Lidar Consortium, Seattle, Washington, U.S.A. available at http://pugetsoundlidar.ess.washington.edu/lidardata/restricted/projects/2016king_county_1.html. 2002 Nisqually Earthquake Shakemap: U.S. Geological Survey (USGS), ShakeMap—Earthquake Ground Motion and Shaking Intensity Maps: USGS available at https://earthquake.usgs.gov/earthquakes/eventpage/uw10530748/shakemap/pgv. All websites were last accessed in September 2020.

DECLARATION OF COMPETING INTERESTS

The authors acknowledge that there are no conflicts of interest recorded.

ACKNOWLEDGMENTS

The authors gratefully acknowledge funding support from National Science Foundation (NSF) Grant Number 1953710 to Duvall and Wirth, Grant Number NSF 2103713 to Duvall and Grant Number NSF 2000188 Booth as well as additional field work and sample analysis support costs to Herzig from the Department of Earth and Space Sciences at the University of Washington. The authors thank Seth Williams for field work assistance. This article was improved by comments and recommendations from Art Frankel and Brian Sherrod and comprehensive reviews by internal U.S. Geological Survey researchers Jon Perkins and Steve Angster. The authors also thank Will Struble, an anonymous reviewer, and associate editor Nicola Litchfield for their thoughtful and indispensable reviews. Any use of trade, firm, or product names is for descriptive purposes only and does not imply endorsement by the U.S. Government.

REFERENCES

Allstadt, K., J. E. Vidale, and A. D. Frankel (2013). A scenario study of seismically induced landsliding in Seattle using broadband synthetic seismograms, *Bull. Seismol. Soc. Am.* **103,** no. 6, 2971–2992.

Angster, S. J., B. L. Sherrod, J. K. Pearl, L. Staisch, and W. Johns (2022). Paleoseismic Evidence for a near historic rupture within the Seattle fault zone: Implications for complex hanging wall kinematics above an active blind reverse fault, *AGU Fall Meeting Abstracts*, Vol. 2022, Chicago, Illinois, 12–16 December 2022, T15B-07.

Atwater, B. F. (1999). Radiocarbon dating of a Seattle earthquake to AD 900–930, *Seismol. Res. Lett.* **70,** no. 2, 232.

Atwater, B. F., and A.L. Moore (1992). A tsunami about 1000 years ago in Puget Sound, Washington, *Science* **258,** no. 5088, 1614–1617.

Aylsworth, J. M., D. E. Lawrence, and J. Guertin (2000). Did two massive earthquakes in the Holocene induce widespread landsliding and near-surface deformation in part of the Ottawa Valley, Canada? *Geology* **28,** no. 10, 903–906.

Baum, R. L., A. F. Chleborad, and R. L. Schuster (1998). Landslides triggered by the winter 1996-97 storms in the Puget Lowland, Washington, *U.S. Geol. Surv. Open-File Rept. 98-239* doi: 10.3133/OFR98239.

Baum, R. L., J. A. Coe, J. W. Godt, E. L. Harp, M. E. Reid, W. Z. Savage, D. L. Brien, A. F. Chleborad, J. P. McKenna, and J. A. Michael (2005). Regional landslide-hazard assessment for Seattle, Washington, USA, *Landslides* **2,** 266–279.

Bird, J. F., and J. J. Bommer (2004). Earthquake losses due to ground failure, *Eng. Geol.* **75,** no. 2, 147–179, doi: 10.1016/j.enggeo.2004.05.006.

Black, B. A., J. K. Pearl, C. L. Pearson, P. T. Pringle, D. C. Frank, M. T. Page, B. M. Buckley, E. R. Cook, G. L. Harley, K. J. Heeter, *et al.* (2023). A multi-fault earthquake threat for the Seattle metropolitan region revealed by mass tree mortality, *Sci. Adv.* **9,** no. 39, eadh4973, doi: 10.1126/sciadv.adh4973.

Blakely, R. J., R. E. Wells, C. S. Weaver, and S. Y. Johnson (2002). Location, structure, and seismicity of the Seattle fault zone, Washington: Evidence from aeromagnetic anomalies, geologic mapping, and seismic-reflection data, *Geol. Soc. Am. Bull.* **114,** 169–177.

Bloom, C. K., A. Howell, T. Stahl, C. Massey, and C. Singeisen (2022). The influence of off-fault deformation zones on the near-fault distribution of coseismic landslides, *Geology* **50,** no. 3, 272–277.

Booth, A. M., S. R. LaHusen, A. R. Duvall, and D. R. Montgomery (2017). Holocene history of deep-seated landsliding in the North Fork Stillaguamish River valley from surface roughness analysis, radiocarbon dating, and numerical landscape evolution modeling, *J. Geophys. Res.* **122,** no. 2, 456–472.

Booth, A. M., J. J. Roering, and T. J. Perron (2009). Automated landslide mapping using spectral analysis and high-resolution

topographic data: Puget Sound lowlands, Washington, and Portland Hills, Oregon, *Geomorphology* **109,** nos. 3/4, 132–147.

Brocher, T. M., T. Parsons, R. J. Blakely, N. I. Christensen, M. A. Fisher, and R. E. Wells (2001). Upper crustal structure in Puget Lowland, Washington: Results from the 1998 seismic hazards investigation in Puget Sound, *J. Geophys. Res.* **106,** no. B7, 13,541–13,564.

Brooks, G. R. (2013). A massive sensitive clay landslide, Quyon valley, southwestern Quebec, Canada, and evidence for a paleoearthquake triggering mechanism, *Quat. Res.* **80,** no. 3, 425–434.

Bucknam, R. C., E. Hemphill-Haley, and E. B. Leopold (1992). Abrupt uplift within the past 1700 years at southern Puget Sound, Washington, *Science* **258,** 1611–1614.

Campforts, B., C. M. Shobe, P. Steer, M. Vanmaercke, D. Lague, and J. Braun (2020). HyLands 1.0: A hybrid landscape evolution model to simulate the impact of landslides and landslide-derived sediment on landscape evolution, *Geosci. Model Dev.* **13,** no. 9, 3863–3886.

Clauset, A., C. R. Shalizi, and M. E. J. Newman (2009). Power-law distributions in empirical data, *SIAM Rev.* **51,** no. 4, 661–703.

Coe, J. A., J. W. Godt, and P. Tachker (2004). *Map Showing Recent (1997-98 El Nino) and Historical Landslides, Crow Creek and Vicinity, Alameda and Contra Costa Counties, California*, U.S. Geological Survey, U.S. Department of the Interior, California, U.S.A.

Croissant, T., P. Steer, D. Lague, P. Davy, L. Jeandet, and R. G. Hilton (2019). Seismic cycles, earthquakes, landslides and sediment fluxes: Linking tectonics to surface processes using a reduced-complexity model, *Geomorphology* **339,** 87–103.

Crozier, M. J., M. S. Deimel, and J. S. Simon (1995). Investigation of earthquake triggering for deep-seated landslides, Taranaki, New Zealand, *Quat. Int.* **25,** 65–73.

Cwynar, L. C. (1987). Fire and the forest history of the North Cascade Range, *Ecology* **68,** no. 4, 791–802.

Davis, E. J., S. Chang, S. Hou, T. Teal, K. Cowell, and S. Garcia-Arceo (2022). A century of landslides in Seattle, Washington: Coalescing and digitizing the City's historic landslide inventories, *Environ. Eng. Geosci.* **28,** no. 4, 335–346.

Fan, X., G. Scaringi, O. Korup, A. J. West, C. J. van Westen, H. Tanyas, N. Hovius, T. C. Hales, R. W. Jibson, K. E. Allstadt, *et al.* (2019). Earthquake-induced chains of geologic hazards: Patterns, mechanisms, and impacts, *Rev. Geophys.* **57,** no. 2, 421–503.

Forero-Duenas, C. A. (1996). Experiences from the Paez earthquake, Colombia, *Eleventh World Conf. on Earthquake Engineering*, Pergamon, Elsevier, Oxford, 23–28 June 1996, paper no. 103.

Francis, O., X. Fan, T. Hales, D. Hobley, Q. Xu, and R. Huang (2022). The fate of sediment after a large earthquake, *J. Geophys. Res.* **127,** no. 3, e2021JF006352, doi: 10.1029/2021JF006352.

Frattini, P., and G. B. Crosta (2013). The role of material properties and landscape morphology on landslide size distributions, *Earth Planet. Sci. Lett.* **361,** 310–319.

Godt, J. W., R. L. Baum, and A. F. Chleborad (2006). Rainfall characteristics for shallow landsliding in Seattle, Washington, USA, *Earth Surf. Process. Landf.* **31,** no. 1, 97–110.

Goetz, J. N., A. Brenning, H. Petschko, and P. Leopold (2015). Evaluating machine learning and statistical prediction techniques for landslide susceptibility modeling, *Comput. Geosci.* **81,** no. B5, doi: 10.1029/2007JB005060.

Goldfinger, C., C. H. Nelson, A. E. Morey, J. E. Johnson, J. R. Patton, E. B. Karabanov, J. Gutierrez-Pastor, A. T. Eriksson, E. Gracia, G. Dunhill, *et al.* (2012). *Turbidite Event History—Methods and Implications for Holocene Paleoseismicity of the Cascadia Subduction Zone, Series No. 1661-F*, U.S. Geological Survey, Reston, Virginia, U.S.A.

Grant, A. (2017). Regional-scale coseismic landslide hazard modeling and consequence analysis, *Doctoral dissertation*, University of Washington.

Grant, A. R., W. T. Struble, and S. R. LaHusen (2022). Limits to coseismic landslides triggered by Cascadia subduction zone earthquakes, *Geomorphology* **418,** 108,477.

Harp, E. L., J. A. Michael, and W. T. Laprade (2008). Shallow landslide hazard map of Seattle, Washington, in *Landslides and Engineering Geology of the Seattle, Washington, Area*, R. L. Baum, J. W. Godt, and L. M. Highland (Editors), Vol. 20, Reviews in Engineering Geology, Geological Society of America, Boulder, Colorado, 67–82.

Highland, L. M. (2003). An account of preliminary landslide damage and losses resulting from the February 28, 2001, Nisqually, Washington, Earthquake, *U.S. Geol. Surv. Open-File Rep. 03–211.*

Hungr, O., S. Leroueil, and L. Picarelli (2014). The Varnes classification of landslide types, an update, *Landslides* **11,** 167–194, doi: 10.1007/s10346-013-0436-y.

Ishihara, K., S. M. Haeri, A. A. Moinfar, I. Towhata, and S. Tsujino (1992). Geotechnical aspects of the June 20, 1990 Manjil earthquake in Iran, *Soils Found.* **32,** no. 3, 61–78.

Jacoby, G. C., P. L. Williams, and B. M. Buckley (1992). Tree ring correlation between prehistoric landslides and abrupt tectonic events in Seattle, Washington, *Science* **258,** no. 5088, 1621–1623.

Jibson, R. W. (1985). Landslides caused by the 1811-12 New Madrid earthquake, *Doctoral dissertation*, Stanford University.

Jibson, R. W. (1996). Use of landslides for paleoseismic analysis, *Eng. Geol.* **43,** no. 4, 291–323.

Jibson, R. W., and D. K. Keefer (1993). Analysis of the seismic origin of landslides: Examples from the New Madrid seismic zone, *Geol. Soc. Am. Bull.* **105,** no. 4, 521–536.

Johnson, S. Y., S. V. Dadisman, J. R. Childs, and W. D. Stanley (1999). Active tectonics of the Seattle fault and central Puget Sound, Washington; Implications for earthquake hazards, *Geol. Soc. Am. Bull.* **111,** 1042–1053.

Johnson, S. Y., C. J. Potter, J. J. Miller, J. M. Armentrout, C. Finn, and C. S. Weaver (1996). The southern Whidbey Island fault: an active structure in the Puget Lowland, Washington, *Geol. Soc. Am. Bull.* **108,** no. 3, 334–354.

Johnson, S. Y., A. R. Nelson, S. F. Personius, R. E. Wells, H. M. Kelsey, B. L. Sherrod, K. Okumura, R. Koehler, R. C. Witter, L. A. Bradley, *et al.* (2004). Evidence for late Holocene earthquakes on the Utsalady Point fault, northern Puget Lowland, Washington, *Bull. Seismol. Soc. Am.* **94,** no. 6, 2299–2316.

Karlin, R. E., M. Holmes, S. E. B. Abella, and R. Sylwester (2004). Holocene landslides and a 3500-year record of Pacific Northwest earthquakes from sediments in Lake Washington, *GSA Bull.* **116,** nos. 1/2, 94–108.

Keefer, D. K. (1984). Landslides caused by earthquakes, *Geol. Soc. Am. Bull.* **95,** no. 4, 406–421.

Kelsey, H. M., B. L. Sherrod, A. R. Nelson, and T. M. Brocher (2008). Earthquakes generated from bedding plane-parallel reverse faults above an active wedge thrust, Seattle fault zone, *Geol. Soc. Am. Bull.* **120,** nos. 11/12, 1581–1597.

Kumar, P., and E. Foufoula-Georgiou (1997). Wavelet analysis for geophysical applications, *Rev. Geophys.* **35,** no. 4, 385–412.

LaHusen, S. R., A. R. Duvall, A. M. Booth, A. Grant, B. A. Mishkin, D. R. Montgomery, W. Struble, J. J. Roering, and J. Wartman (2020). Rainfall triggers more deep-seated landslides than Cascadia earthquakes in the Oregon Coast Range, USA, *Sci. Adv.* **6,** no. 38, eaba6790, doi: 10.1126/sciadv.aba6790.

LaHusen, S. R., A. R. Duvall, A. M. Booth, and D. R. Montgomery (2016). Surface roughness dating of long-runout landslides near Oso, Washington (USA), reveals persistent postglacial hillslope instability, *Geology* **44,** no. 2, 111–114.

Laprade, W. T., T. E. Kirkland, W. D. Nashem, and C. A. Robertson (2000). *Seattle Landslide Study, Internal Rept. W-7992 1*, Shannon and Wilson, Inc., Seattle, Washington, 83 pp.

Lashermes, B., E. Foufoula-Georgiou, and W. E. Dietrich (2007). Channel network extraction from high resolution topography using wavelets, *Geophys. Res. Lett.* **34,** no. 23, doi: 10.1029/2007GL031140.

Ludwin, R. S., C. P. Thrush, K. James, D. Buerge, C. Jonientz-Trisler, J. Rasmussen, K. Troost, and A. De Los Angeles (2005). Serpent spirit-power stories along the Seattle fault, *Seismol. Res. Lett.* **76,** no. 4, 426–431.

Luna, L. V., and O. Korup (2022). Seasonal landslide activity lags annual precipitation pattern in the Pacific northwest, *Geophys. Res. Lett.* **49,** no. 18, e2022GL098506, doi: 10.1029/2022GL098506.

Malamud, B. D., D. L. Turcotte, F. Guzzetti, and P. Reichenbach (2004). Landslide inventories and their statistical properties, *Earth Surf. Process. Landf.* **29,** no. 6, 687–711.

Marc, O., N. Hovius, and P. Meunier (2016). The mass balance of earthquakes and earthquake sequences, *Geophys. Res. Lett.* **43,** no. 8, 3708–3716.

Massey, F. J. (1951). The Kolmogorov-Smirnov test for goodness of fit, *J. Am. Stat. Assoc.* **46,** no. 253, 68–78.

McKean, J., and J. Roering (2004). Objective landslide detection and surface morphology mapping using high-resolution airborne laser altimetry, *Geomorphology* **57,** nos. 3/4, 331–351.

Medwedeff, W. G., M. K. Clark, D. Zekkos, and A. J. West (2020). Characteristic landslide distributions: An investigation of landscape controls on landslide size, *Earth Planet. Sci. Lett.* **539,** 116,203.

Meunier, P., N. Hovius, and J. A. Haines (2008). Topographic site effects and the location of earthquake induced landslides, *Earth Planet. Sci. Lett.* **275,** nos. 3/4, 221–232.

Moore, G. L., E. Roland, S. E. Bennett, J. Watt, J. Kluesner, D. Brothers, and E. Myers (2022). High-resolution marine seismic imaging of the Seattle fault zone: Near-surface insights into fault zone geometry, quaternary deformation, and long-term evolution, *Bull. Seismol. Soc. Am.* **112,** no. 5, 2715–2744.

Nelson, A. R., S. Y. Johnson, H. M. Kelsey, R. E. Wells, B. L. Sherrod, S. K. Pezzopane, L. A. Bradley, R. D. Koehler, and R. C. Bucknam (2003). Late Holocene earthquakes on the Toe Jam Hill fault, Seattle fault zone, Bainbridge Island, Washington, *Geol. Soc. Am. Bull.* **115,** no. 11, 1388–1403.

Nelson, A. R., S. F. Personius, B. L. Sherrod, H. M. Kelsey, S. Y. Johnson, L. A. Bradley, and R. E. Wells (2014). Diverse rupture modes for surface-deforming upper plate earthquakes in the southern Puget Lowland of Washington State, *Geosphere* **10,** no. 4, 769–796.

Pánek, T. (2015). Recent progress in landslide dating: A global overview, *Prog. Phys. Geogr.* **39,** no. 2, 168–198.

Parker, R. N., G. T. Hancox, D. N. Petley, C. I. Massey, A. L. Densmore, and N. J. Rosser (2015). Spatial distributions of earthquake-induced landslides and hillslope preconditioning in the northwest South Island, New Zealand, *Earth Surf. Dynam.* **3,** no. 4, 501–525.

Perkins, J. P., M. E. Reid, and K. M. Schmidt (2017). Control of landslide volume and hazard by glacial stratigraphic architecture, northwest Washington State, USA, *Geology* **45,** no. 12, 1139–1142.

Pollock, W., A. Grant, J. Wartman, and G. Abou-Jaoude (2019). Multimodal method for landslide risk analysis, *MethodsX* **6,** 827–836.

Pratt, T. L., S. Y. Johnson, C. J. Potter, W. J. Stephenson, and C. A. Finn (1997). Seismic reflection images beneath Puget Sound, western Washington State: The Puget Lowland thrust sheet hypothesis, *J. Geophys. Res.* **102,** 27,469–27,489.

Ramsey, C. B. (2009). Bayesian analysis of radiocarbon dates, *Radiocarbon* **51,** no. 1, 337–360.

Ramsey, C. B. (2017). Methods for summarizing radiocarbon datasets, *Radiocarbon* **59,** no. 6, 1809–1833.

Rasanen, R. A., and B. W. Maurer (2021). Probabilistic seismic source inversion from regional landslide evidence, *Landslides* **19,** 407–419.

Reimer, P. J., E. Bard, A. Bayliss, J. W. Beck, P. G. Blackwell, C. B. Ramsey, C. E. Buck, H. Cheng, R. L. Edwards, M. Friedrich, *et al.* 2013)). IntCal13 and Marine13 radiocarbon age calibration curves 0–50,000 years cal BP, *Radiocarbon* **55,** no. 4, 1869–1887.

Ricker, N. (1943). Further developments in the wavelet theory of seismogram structure, *Bull. Seismol. Soc. Am.* **33,** no. 3, 197–228.

Sadler, P. M. (1981). Sediment accumulation rates and the completeness of stratigraphic sections, *J. Geol.* **89,** no. 5, 569–584.

Schulz, W. H. (2007). Landslide susceptibility revealed by LIDAR imagery and historical records, Seattle, Washington, *Eng. Geol.* **89,** nos. 1/2, 67–87.

Schulz, W. H., S. L. Galloway, and J. D. Higgins (2012). Evidence for earthquake triggering of large landslides in coastal Oregon, USA, *Geomorphology* **141,** 88–98.

Schumer, R., and D. J. Jerolmack (2009). Real and apparent changes in sediment deposition rates through time, *J. Geophys. Res.* **114,** no. F3, doi: 10.1029/2009JF001266.

Schuster, R. L., R. L. Logan, and P. T. Pringle (1992). Prehistoric rock avalanches in the Olympic Mountains, Washington, *Science* **258,** no. 5088, 1620–1621.

Serey, A., L. Piñero-Feliciangeli, S. A. Sepúlveda, F. Poblete, D. N. Petley, and W. Murphy (2019). Landslides induced by the 2010 Chile megathrust earthquake: A comprehensive inventory and correlations with geological and seismic factors, *Landslides* **16,** 1153–1165.

Sherrod, B. L. (2001). Evidence for earthquake-induced subsidence about 1100 yr ago in coastal marshes of southern Puget Sound, Washington, *GSA Bull.* **113,** no. 10, 1299–1311.

Sherrod, B. L., R. J. Blakely, C. S. Weaver, H. M. Kelsey, E. Barnett, L. Liberty, K. L. Meagher, and K. Pape (2008). Finding concealed active faults: Extending the southern Whidbey Island fault across the Puget Lowland, Washington, *J. Geophys. Res.* **113,** no. B5, doi: 10.1029/2007JB005060.

Sherrod, B. L., T. M. Brocher, C. S. Weaver, R. C. Bucknam, R. J. Blakely, H. M. Kelsey, A. R. Nelson, and R. Haugerud (2004). Holocene fault scarps near Tacoma, Washington, USA. *Geology* **32,** no. 1, 9–12.

Sherrod, B. L., R. C. Bucknam, and E. B. Leopold (2000). Holocene relative sea level changes along the Seattle fault at restoration point, Washington, *Quat. Res.* **54,** no. 3, 384–93.

Stone, I., E. A. Wirth, and A. D. Frankel (2022). Topographic response to simulated M w 6.5–7.0 earthquakes on the Seattle fault, *Bull. Seismol. Soc. Am.* **112,** no. 3, 1436–1462.

Struble, W. T., J. J. Roering, B. A. Black, W. J. Burns, N. Calhoun, and L. Wetherell (2020). Dendrochronological dating of landslides in western Oregon: Searching for signals of the Cascadia AD 1700 earthquake, *GSA Bull.* **132,** nos. 7/8, 1775–1791.

Styron, R. H., and B. Sherrod (2021). Improving paleoseismic earthquake magnitude estimates with rupture length information: Application to the Puget Lowland, Washington State, USA, *Bull. Seismol. Soc. Am.* **111,** no. 2, 1139–1153.

Tanyas, H., K. E. Allstadt, and C. J. van Westen (2018). An updated method for estimating landslide-event magnitude, *Earth Surf. Process. Landf.* **43,** no. 9, 1836-1847.

ten Brink, U. S., P. C. Molzer, M. A. Fisher, R. J. Blakely, R. C. Bucknam, T. Parsons, R. S. Crosson, and K. C. Creager (2002). Subsurface geometry and evolution of the Seattle fault zone and the Seattle basin, Washington, *Bull. Seismol. Soc. Am.* **92,** 1737–1753.

ten Brink, U. S., J. Song, and R. C. Bucknam (2006). Rupture models for the AD 900–930 Seattle fault earthquake from uplifted shorelines, *Geology* **34,** no. 7, 585–588.

Tubbs, D. W. (1974). *Landslides in Seattle*, Department of Natural Resources, Olympia, Washington, D.C.

Valagussa, A., O. Marc, P. Frattini, and G. B. Crosta (2019). Seismic and geological controls on earthquake-induced landslide size, *Earth Planet. Sci. Lett.* **506,** 268–281.

Wang, J., J. D. Howarth, E. L. McClymont, A. L. Densmore, S. J. Fitzsimons, T. Croissant, D. R. Gröcke, M. D. West, E. L. Harvey, N. V. Frith, *et al.* (2020). Long-term patterns of hillslope erosion by earthquake-induced landslides shape mountain landscapes, *Sci. Adv.* **6,** no. 23, eaaz6446, doi: 10.1126/sciadv.aaz6446.

Wartman, J., L. Dunham, B. Tiwari, and D. Pradel (2013). Landslides in eastern Honshu induced by the 2011 Tohoku earthquake, *Bull. Seismol. Soc. Am.* **103,** no. 2B, 1503–1521, doi: 10.1785/0120120128.

Washington Geological Survey (2020). Landslide protocol inventory mapping—GIS data, February, 2020: *Washington Geological Survey Digital Data Series 19*, version 2.0, previously released January 2019, available at https://fortress.wa.gov/dnr/geologydata/publications/data_download/ger_portal_landslide_database.zip (last accessed June 2020).

Yount, J. C., J. P. Minard, and G. R. Dembroff (1993). *Geologic Map of Surficial Deposits in the Seattle 30′ × 60′ quadrangle, Open-File Rept. 93-233*, U.S. Geological Survey, Washington, D.C.

Manuscript received 19 April 2023
Published online 7 November 2023